Acta Geotechnica (2015) 10:83–100
DOI 10.1007/s11440-014-0342-z

RESEARCH PAPER

Flow liquefaction instability prediction using finite elements

Toktam Mohammadnejad · José E. Andrade

Received: 14 November 2013 / Accepted: 6 June 2014 / Published online: 30 July 2014

Abstract In this paper, a mathematical criterion based on bifurcation theory is developed to predict the onset of liquefaction instability in fully saturated porous media under static and dynamic loading conditions. The proposed liquefaction criterion is general and can be applied to any elastoplastic constitutive model. Since the liquefaction criterion is only as accurate as the underlying constitutive model utilized, the modified Manzari–Dafalias model is chosen for its accuracy, relative simplicity and elegance. Moreover, a fully implicit return mapping algorithm is developed for the numerical implementation of the Manzari–Dafalias model, and a consistent tangent operator is derived to obtain optimal convergence with finite elements. The accuracy of the implementation is benchmarked against laboratory experiments under monotonic and cyclic loading conditions, and a qualitative boundary value problem. The framework is expected to serve as a tool to enable prediction of liquefaction occurrence in the field under general static and dynamic conditions. Further, the methodology can help advance our understanding of the phenomenon in the field as it can clearly differentiate between unstable behavior, such as flow liquefaction, and material failure, such as cyclic mobility.

Keywords Finite element analysis · Fully implicit return mapping algorithm · Granular materials · Liquefaction instability · Manzari–Dafalias plasticity model · Static and dynamic liquefaction

T. Mohammadnejad · J. E. Andrade (✉)
Mechanical and Civil Engineering, California Institute of Technology, Pasadena, CA, USA
e-mail: jandrade@caltech.edu

1 Introduction

Liquefaction—as an instability phenomenon—is perhaps one of the most devastating yet elusive concepts in geotechnical engineering. Abundant field evidence shows a sudden loss of shear strength typically associated with an apparent build-up of pore water pressure, usually observed in relatively loose cohesionless soil formations. Several case studies from earthquakes around the globe have shown the world the devastating power of liquefaction: Niigata 1964, Kobe 1995, Haiti 2010, and Christchurch 2011, among others. Yet, very little is known about the mechanisms controlling the phenomenon to the extent that predictive models have remained elusive. In fact, for many years, the liquefaction phenomenon was associated solely as a result of earthquake (cyclic) loading and confounded with cyclic mobility.

It is now widely accepted that: (1) liquefaction is an instability (usually termed 'flow liquefaction,' see [14]) and (2) it can occur under static or dynamic conditions (the former is typically called 'static liquefaction'). Several works in the field have shown the unstable behavior of the material in the laboratory under static and cyclic loading conditions [7, 15, 27]. Based on Hill's instability criterion [11], Lade [15] showed that there exists an 'instability line' that connects the points at which the material loses stability in the laboratory under undrained conditions and quasi-static loading. Borja [5] postulated a condition for liquefaction instability, and Andrade [1] simplified the latter condition and applied it to elastoplastic models, extracting in this way a simple critical hardening modulus pinpointing the onset of liquefaction, which coincides with the instability line of Lade [15] and the concept of 'loss of controllability' postulated by Nova [22]. Later, Andrade et al. [3] built on the concept of instability and expanded the

liquefaction criterion to dynamic (cyclic) loading. In their work, it was shown that liquefaction flow (or simply liquefaction) is an instability, whereas cyclic mobility is a failure phenomenon resulting from material response, but it is not an instability. In this way, they showed the fundamental difference between liquefaction (as an instability) and cyclic mobility.

Most, if not all, the aforementioned works are based on laboratory scale observations. Once the jump to the field scale, most of the works become observational, with potential failure mechanisms postulated to reconstruct the observed failure patterns. The classic example is the failure of the lower San Fernando dam in 1971, which was remarkably reconstructed by Seed et al. [25]. In an attempt to provide a quantitative and rational approach, Zienkiewicz et al. [30] developed a finite element model based on elastoplasticity, where they showed some qualitative and limited quantitative agreement with the observations made for the lower San Fernando dam. Most remarkable is their prediction of the deformation pattern as a result of the earthquake excitation and capturing of the 'delay' in failure, occurring approximately 60 s after the earthquake. Nevertheless, the field-scale approach based on finite elements has lacked a proper criterion for liquefaction and correspondingly robust constitutive models to make the predictions plausible.

As a first attempt to map liquefaction instabilities, Ellison and Andrade [10] developed a finite element model based on the mixed formulation to simulate static liquefaction and were able to reproduce a classic example previously postulated by Lade [15] for submarine levees. However, the solution is quasi-static, and it is not capable to shed full light into the dynamic regime. This work is based on the liquefaction criterion of Andrade [1] and the mixed finite element for saturated granular materials under static conditions proposed by Andrade and Borja [2].

In this contribution, the liquefaction criterion is further generalized from that of Andrade et al. [3] to general loading conditions (as opposed to triaxial (axisymmetric) loading). In that way, the criterion proposed herein is closer in philosophy to the one obtained by Borja [5] under static conditions. The proposed criterion is applied to the most recent Dafalias and Manzari model for sands [9], which captures accurately the cyclic behavior of the material invoking elastoplasticity. The Manzari–Dafalias plasticity model with recent modifications is numerically integrated using a fully implicit return mapping algorithm. The implicit integration of the original model or slight variations of the model can be found in [8, 16, 21]. Finally, the model and corresponding liquefaction criterion are cast into a dynamic finite element code capable of simulating coupled soil deformation with fluid flow using the classic u-p formulation. In this way, this paper presents the fully implicit implementation of the Manzari–Dafalias model within a finite element code with the capability of mapping the onset of liquefaction instability under dynamic conditions. The accuracy of the implementation is benchmarked against laboratory experiments under monotonic and cyclic loading conditions, and a boundary value problem under dynamic loading conditions. The framework is expected to serve as a tool to enable prediction of liquefaction occurrence in the field under general loading conditions. As such, the current paper should not be interpreted to applying uniquely to the Manzari–Dafalias model, but can be used with any other elastoplasticity model in the field. The authors have chosen the aforementioned model for its capabilities, relative simplicity, and elegance, but this is a personal choice.

The structure of the paper is as follows. In Sect. 2, the equations governing the problem are summarized. In Sect. 3, the Manzari–Dafalias plasticity model based on its recent modifications is briefly described. In Sect. 4, a fully implicit integration scheme is developed for the numerical implementation of the Manzari–Dafalias plasticity model, and a consistent tangent operator relevant to the proposed return mapping algorithm is presented. In Sect. 5, a general, mathematical criterion for the onset of liquefaction instability is obtained. In Sect. 6, the capability of the proposed criterion in capturing the onset of liquefaction instability under monotonic and cyclic loading conditions is demonstrated by solving a number of triaxial tests, and its applicability to boundary value problems under dynamic loading conditions is shown through a fully coupled dynamic analysis of a plane strain test. Finally, conclusion is made in the last section.

2 Governing equations

In this section, governing equations of fully saturated porous media are presented. These governing equations are based on two basic laws of force equilibrium and mass conservation. For numerical solution of the governing equations, finite element method is employed to discretize the weak form of the governing equations in space together with the generalized Newmark scheme for time domain discretization.

2.1 Strong form of the governing equations

The partial differential equations governing the solid phase deformation and pore fluid flow through the porous medium are based on the balance equations of linear momentum and mass. The linear momentum balance equation for a fully saturated porous medium can be written as [17]

$$\nabla \cdot \boldsymbol{\sigma} + \rho \mathbf{b} - \rho \ddot{\mathbf{u}} = \mathbf{0} \tag{1}$$

where $\boldsymbol{\sigma}$ is the total stress tensor defined as $\boldsymbol{\sigma} = \boldsymbol{\sigma}'' - \alpha p_w \mathbf{I}$, with $\boldsymbol{\sigma}''$ the modified effective stress tensor, α the Biot constant, p_w the pore fluid pressure, and $\mathbf{I}$ the second-order identity tensor, $\mathbf{b}$ is the body force vector, $\ddot{\mathbf{u}}$ is the acceleration vector of the solid phase, ρ is the average density of the whole mixture defined as $\rho = (1-n)\rho_s + n\rho_w$, in which n stands for the porosity of the porous medium and ρ_s and ρ_w are densities of solid and fluid phases, respectively, and the symbol ∇ denotes the vector gradient operator. Throughout this paper, the mechanics convention is used, where stress is considered positive in tension, while the pore fluid pressure is considered as compression positive.

The continuity equation for pore fluid flow through a fully saturated porous medium can be written as [17]

$$\left(\frac{\alpha - n}{K_s} + \frac{n}{K_w}\right)\dot{p}_w + \alpha \nabla \cdot \dot{\mathbf{u}} + \nabla \cdot \dot{\mathbf{w}}_w = 0 \tag{2}$$

where K_s and K_w are bulk moduli of solid and fluid phases, respectively, $\dot{\mathbf{u}}$ is the velocity vector of the solid phase, and $\dot{\mathbf{w}}_w$ is the Darcy's velocity vector of the pore fluid given by $\dot{\mathbf{w}}_w = (\mathbf{k}/\mu_w)[-\nabla p_w + \rho_w(\mathbf{b} - \ddot{\mathbf{u}})]$ with $\mathbf{k}$ the intrinsic permeability matrix of the porous medium, simply replaced by a scalar value k for an isotropic medium, and μ_w the dynamic viscosity of the pore fluid.

2.2 Discrete form of the governing equations

The finite element approximation of the primary unknown variables can be written as [17]

$$\begin{aligned} \mathbf{u}^h(\mathbf{x}, t) &= \mathbf{N}_u(\mathbf{x})\mathbf{U}(t) \\ p_w^h(\mathbf{x}, t) &= \mathbf{N}_{p_w}(\mathbf{x})\mathbf{P}_w(t) \end{aligned} \tag{3}$$

where $\mathbf{N}_u(\mathbf{x})$ and $\mathbf{N}_{p_w}(\mathbf{x})$ are matrices of finite element shape functions and $\mathbf{U}(t)$ and $\mathbf{P}_w(t)$ are vectors of displacement and pressure degrees of freedom, respectively. It is worth noting that if the incompressible and undrained limit state is never approached, equal-order shape functions can be used for the approximation of both solid and fluid variables. Otherwise, it is necessary that the displacement field be approximated by polynomial shape functions one order higher than those used for the approximation of the pressure field [17]. Different order of shape functions prevents spurious oscillations and locking in the pressure field in the limit of nearly incompressible and undrained state.

Following the Bubnov–Galerkin technique, the discretized form of the governing Eqs. (1) and (2) is obtained as

$$\begin{aligned} \mathbf{M}_u \ddot{\mathbf{U}} + \int_\Omega \mathbf{B}^{\mathrm{T}} \boldsymbol{\sigma}'' \, \mathrm{d}\Omega - \mathbf{Q}\mathbf{p}_w &= \mathbf{F}_u \\ \mathbf{M}_w \ddot{\mathbf{U}} + \mathbf{Q}^{\mathrm{T}} \dot{\mathbf{U}} + \mathbf{C}\dot{\mathbf{p}}_w + \mathbf{H}\mathbf{p}_w &= \mathbf{F}_w \end{aligned} \tag{4}$$

where $\mathbf{B}$ is the strain–displacement matrix. The definition of the coefficient matrices and the force and flux vectors is given in 'Appendix 1.' The above system of equations is then discretized in time following the line of the well-known Newmark scheme. The resulting system of fully coupled nonlinear equations is solved using the unconditionally stable direct time-stepping procedure combined with the Newton–Raphson iterative process. As a result, the main unknowns are obtained simultaneously, leading to the full solution of the problem. For a detailed presentation of the solution procedure, see [13].

3 Constitutive model

In order to simulate the mechanical behavior of the granular material, the Manzari–Dafalias plasticity model is used. This model was originally proposed in [20] and then was extended to account for the effect of fabric changes during the dilative phase of deformation on the subsequent contractive phase upon loading reversal [9]. The Manzari–Dafalias constitutive model is framed within the context of the critical state soil mechanics [24], which is based on the theory that for a given soil, a unique critical state line (CSL) exists. In the following, the Manzari–Dafalias plasticity model [9] is briefly described.

In Manzari–Dafalias plasticity model, the nonlinear elastic response of the material is described by the hypo-elastic formulation. The volumetric and deviatoric part of the elastic strain rate tensor are given by

$$\dot{\varepsilon}_v^e = -\frac{\dot{p}}{K}, \quad \dot{\mathbf{e}}^e = \frac{\dot{\mathbf{s}}}{2G} \tag{5}$$

where $\dot{\varepsilon}_v^e = \mathrm{tr}\,\dot{\boldsymbol{\varepsilon}}^e, \dot{\mathbf{e}}^e = \dot{\boldsymbol{\varepsilon}}^e - \dot{\varepsilon}_v^e/3\mathbf{I}$, p is the mean effective stress defined as $p = -\mathrm{tr}\,\boldsymbol{\sigma}''/3$, $\mathbf{s}$ is the deviatoric effective stress tensor defined as $\mathbf{s} = \boldsymbol{\sigma}'' + p\mathbf{I}$, and K and G are the elastic bulk and shear moduli, respectively, which are the functions of the mean effective stress and void ratio [18, 23]

$$K = \frac{2(1+\upsilon)}{3(1-2\upsilon)}G, \quad G = G_0 p_{\mathrm{at}} \frac{(2.97-e)^2}{(1+e)}\left(\frac{p}{p_{\mathrm{at}}}\right)^{1/2} \tag{6}$$

where υ is the Poisson's ratio, G_0 is a material constant, p_{at} is the atmospheric pressure and e is the void ratio whose evolution is given by $\dot{e} = (1+e)\dot{\varepsilon}_v$, with $\dot{\varepsilon}_v = \mathrm{tr}\,\dot{\boldsymbol{\varepsilon}}$ the volumetric strain rate.

The yield surface is defined by

$$f\left(\boldsymbol{\sigma}'', \boldsymbol{\alpha}\right) = [(\mathbf{s} - p\boldsymbol{\alpha}):(\mathbf{s} - p\boldsymbol{\alpha})]^{1/2} - \sqrt{2/3}\, pm = 0 \tag{7}$$

which geometrically represents a circular cone whose apex is at the origin in the effective stress space. The yield surface determines the limit of the elastic domain. In the above relation, $\boldsymbol{\alpha}$ is the deviatoric back stress-ratio tensor defining the orientation of the cone, m is a constant defining the size of the cone, and the symbol ':' denotes the inner product of two second-order tensors. The evolution of $\boldsymbol{\alpha}$ is governed by the kinematic hardening law as

$$\dot{\boldsymbol{\alpha}} = \langle \dot{L} \rangle (2/3) h \mathbf{b} \tag{8}$$

where L is the loading index, the symbol $\langle\rangle$ denotes the Macaulay brackets, and h is the hardening coefficient, which is positive, and given by

$$h = \frac{b_0}{(\boldsymbol{\alpha} - \boldsymbol{\alpha}_{\text{in}}):\mathbf{n}}, \quad b_0 = G_0 h_0 (1 - c_h e) \left(\frac{p}{p_{\text{at}}}\right)^{-1/2} \tag{9}$$

In the above relation, $\boldsymbol{\alpha}_{\text{in}}$ is the initial value of $\boldsymbol{\alpha}$ at the initiation of a new loading process and is updated when $(\boldsymbol{\alpha} - \boldsymbol{\alpha}_{\text{in}}):\mathbf{n}$ becomes negative, $\mathbf{n}$ is the unit deviatoric tensor, which is equal to the deviatoric part of the normal to the yield surface, and h_0 and c_h are positive constants. The unit deviatoric tensor $\mathbf{n}$ is defined as $\mathbf{n} = (\mathbf{s} - p\boldsymbol{\alpha})/\|\mathbf{s} - p\boldsymbol{\alpha}\|$, in which the symbol $\| \ \|$ denotes the L_2 norm of a tensor. It is obvious that the unit deviatoric tensor $\mathbf{n}$ has the following properties: $\text{tr}\,\mathbf{n} = 0$ and $\mathbf{n}:\mathbf{n} = 1$. In Eq. (8), $\mathbf{b}$ is given by

$$\mathbf{b} = \sqrt{2/3}\alpha_\theta^b \mathbf{n} - \boldsymbol{\alpha}, \quad \alpha_\theta^b = M \exp\left(-n^b \psi\right) - m \tag{10}$$

where n^b is a positive material constant, $\psi = e - e_{\text{c}}$ is the state parameter, in which e_{c} is the critical void ratio corresponding to the existing mean effective stress computed from the power relation proposed by Li and Wang [19]

$$e_{\text{c}} = e_{\text{c0}} - \lambda_{\text{c}} (p/p_{\text{at}})^{\xi} \tag{11}$$

with e_{c0}, λ_{c} and ξ constants. In Eq. (10), M is the critical state stress ratio obtained by

$$M = g(\theta, c) M_{\text{c}}, \quad g(\theta, c) = \frac{2c}{(1 + c) - (1 - c)\cos 3\theta} \tag{12}$$

where θ is an effective Lode angle whose value varies from 0 to $\pi/3$ defined by $\cos 3\theta = -\sqrt{6}\,\text{tr}\mathbf{n}^3$ and $c = M_{\text{e}}/M_{\text{c}}$ with M_{c} and M_{e} the triaxial compression and extension critical state stress ratios, respectively.

The plastic strain rate tensor is given by

$$\dot{\boldsymbol{\varepsilon}}^p = \langle \dot{L} \rangle \mathbf{R}, \qquad \mathbf{R} = B\mathbf{n} + C\left(\mathbf{n}^2 - \frac{1}{3}\mathbf{I}\right) - \frac{1}{3} D \mathbf{I} \tag{13}$$

where $\mathbf{R}$ determines the direction of plastic flow, $B = 1 + 3(1 - c)/(2c) g(\theta, c) \cos 3\theta$, $C = 3\sqrt{3/2}(1 - c)/c g(\theta, c)$ and D is the dilatancy defined by

$$D = A_d \mathbf{d}:\mathbf{n}, \qquad A_d = A_0 (1 + \langle \mathbf{z}:\mathbf{n} \rangle) \tag{14}$$

where A_0 is a positive constant and $\mathbf{z}$ is the so-called fabric-dilatancy tensor whose evolution is governed by

$$\dot{\mathbf{z}} = -c_z \langle \dot{L} \rangle \langle -D \rangle (z_{\max} \mathbf{n} + \mathbf{z}) \tag{15}$$

with c_z and $z_{\max}$ material constants. The above equation implies that the evolution of $\mathbf{z}$ occurs during the dilative phase of deformation. In Eq. (14), $\mathbf{d}$ is given by

$$\mathbf{d} = \sqrt{2/3}\alpha_\theta^d \mathbf{n} - \boldsymbol{\alpha}, \quad \alpha_\theta^d = M \exp\left(n^d \psi\right) - m \tag{16}$$

where n^d is a positive material constant.

4 Numerical implementation

In this section, a fully implicit return mapping algorithm is developed for the most recent plasticity model for sands by Dafalias and Manzari [9], in which the Newton–Raphson scheme is employed to iteratively arrive at a solution satisfying all the constitutive equations at the local level. Furthermore, a consistent tangent operator relevant to the proposed return mapping algorithm is derived by exploiting the converged residual vector. In what follows, Voigt notation is used. Following this, a second-order tensor is reduced to a six-dimensional vector and a forth-order tensor is reduced to a 6×6 matrix.

4.1 Implicit return mapping algorithm

Assuming that the strain increment at time t_{n+1}, that is $\Delta\boldsymbol{\varepsilon}$, is given, the current strain can be directly computed from $\boldsymbol{\varepsilon} = \boldsymbol{\varepsilon}_n + \Delta\boldsymbol{\varepsilon}$, in which $\boldsymbol{\varepsilon}_n$ is the strain vector at time t_n which is known, and the current void ratio can be obtained by integrating its evolution equation given in the previous section, i.e., $e = (1 + e_n)\exp(\Delta\varepsilon_{\text{v}}) - 1$, with $\Delta\varepsilon_{\text{v}} = \text{tr}\,\Delta\boldsymbol{\varepsilon}$ the volumetric strain increment. It is noted that throughout this section, the subscript $n + 1$ is assumed for variables without subscript. The objective is to find the stress vector $\boldsymbol{\sigma}''$ corresponding to the given strain increment $\Delta\boldsymbol{\varepsilon}$. Initially, i.e., at iteration $i = 0$, the material response is assumed to be elastic ($\Delta\boldsymbol{\varepsilon}^{e,0} = \Delta\boldsymbol{\varepsilon}$), that is

$$\begin{aligned} &\boldsymbol{\varepsilon}^{e,0} = \boldsymbol{\varepsilon}^{e,\text{tr}} = \boldsymbol{\varepsilon}_n^e + \Delta\boldsymbol{\varepsilon} \\ &\boldsymbol{\alpha}^0 = \boldsymbol{\alpha}_n \\ &\mathbf{z}^0 = \mathbf{z}_n \\ &\Delta L^0 = 0 \end{aligned} \tag{17}$$

where $\boldsymbol{\varepsilon}^{e,\mathrm{tr}}$ is the trial elastic strain. The trial stress is obtained by integrating the rate equation $\dot{\boldsymbol{\sigma}}'' = \mathbf{C}^e \cdot \dot{\boldsymbol{\varepsilon}}^e$ using the Euler scheme

$$\boldsymbol{\sigma}''^{,0} = \boldsymbol{\sigma}''^{,\mathrm{tr}} = \boldsymbol{\sigma}''_n + \mathbf{C}^{e,0} \cdot \Delta\boldsymbol{\varepsilon} \tag{18}$$

where $\boldsymbol{\sigma}''_n$ is the stress vector at time t_n which is known, and $\mathbf{C}^{e,0}$ is the trial elasticity matrix, in which the trial bulk and shear moduli are evaluated from Eq. (6) as follows

$$K^0 = \frac{2(1+\upsilon)}{3(1-2\upsilon)} G^0, \quad G^0 = G_0 p_{\mathrm{at}} \frac{(2.97-e)^2}{(1+e)} \left(\frac{p^0}{p_{\mathrm{at}}}\right)^{1/2} \tag{19}$$

where p^0 is the trial mean effective stress obtained by integrating the volumetric part of the elastic relation given in Eq. (5)

$$p^0 = \left(p_n^{1/2} - \frac{(1+\upsilon)}{3(1-2\upsilon)} \mathrm{G}_0 p_{\mathrm{at}}^{1/2} \frac{(2.97-e)^2}{(1+e)} \Delta\varepsilon_{\mathrm{v}} \right)^2 \tag{20}$$

If the trial stress state is located inside or on the yield surface, that is

$$f\left(\boldsymbol{\sigma}''^{,0}, \boldsymbol{\alpha}^0\right) = \left[\left(\mathbf{s}^0 - p^0\boldsymbol{\alpha}^0\right) \cdot \left(\mathbf{s}^0 - p^0\boldsymbol{\alpha}^0\right) \right]^{1/2} - \sqrt{2/3} p^0 m \leq 0 \tag{21}$$

elastic prediction is correct.

If the trial stress state obtained using the elastic prediction is located outside the yield surface, that is $f\left(\boldsymbol{\sigma}''^{,0}, \boldsymbol{\alpha}^0\right) > 0$, the trial state is corrected by simultaneously satisfying the following equations, which are generated by the strain increment $\Delta\boldsymbol{\varepsilon}$

$$\mathbf{r} = \begin{Bmatrix} \mathbf{r}_{\varepsilon^e} \\ \mathbf{r}_{\alpha} \\ \mathbf{r}_{z} \\ \mathrm{r}_{\Delta L} \end{Bmatrix} = \begin{Bmatrix} \boldsymbol{\varepsilon}^e - \boldsymbol{\varepsilon}^{e,\mathrm{tr}} + \Delta L \mathbf{R} \\ \boldsymbol{\alpha} - \boldsymbol{\alpha}_n - \Delta L (2/3) h \mathbf{b} \\ \mathbf{z} - \mathbf{z}_n + c_z \Delta L \langle -D \rangle (z_{\max}\mathbf{n} + \mathbf{z}) \\ \left[(\mathbf{s} - p\boldsymbol{\alpha}) \cdot (\mathbf{s} - p\boldsymbol{\alpha}) \right]^{1/2} - \sqrt{2/3} p m \end{Bmatrix} = \mathbf{0} \tag{22}$$

These equations involve the additive decomposition of the strain rate tensor into elastic and plastic parts, i.e., $\dot{\boldsymbol{\varepsilon}} = \dot{\boldsymbol{\varepsilon}}^e + \dot{\boldsymbol{\varepsilon}}^p$, the evolution of the deviatoric back stress-ratio tensor $\boldsymbol{\alpha}$ [Eq. (8)], the evolution of the fabric-dilatancy tensor $\mathbf{z}$ [Eq. (15)], and the yield condition [Eq. (7)].

In order to solve the above system of equations, the Newton–Raphson iterative scheme is implemented to linearize the above system of equations. By expanding the local residual equations with the first-order truncated Taylor series, the following linear approximation is obtained for the nonlinear system to be solved

$$\begin{Bmatrix} \mathbf{r}_{\varepsilon^e}^{i+1} \\ \mathbf{r}_{\alpha}^{i+1} \\ \mathbf{r}_{z}^{i+1} \\ \mathrm{r}_{\Delta L}^{i+1} \end{Bmatrix} = \begin{Bmatrix} \mathbf{r}_{\varepsilon^e}^{i} \\ \mathbf{r}_{\alpha}^{i} \\ \mathbf{r}_{z}^{i} \\ \mathrm{r}_{\Delta L}^{i} \end{Bmatrix} + \mathbf{J}^i \cdot \begin{Bmatrix} \mathrm{d}\boldsymbol{\varepsilon}^{e,i+1} \\ \mathrm{d}\boldsymbol{\alpha}^{i+1} \\ \mathrm{d}\mathbf{z}^{i+1} \\ \mathrm{d}\Delta L^{i+1} \end{Bmatrix} = \mathbf{0} \tag{23}$$

which can be rewritten as

$$\mathbf{r}^{i+1} = \mathbf{r}^i + \mathbf{J}^i \cdot \mathrm{d}\mathbf{X}^{i+1} = \mathbf{0} \tag{24}$$

where $\mathbf{X} = \left[(\boldsymbol{\varepsilon}^e)^{\mathrm{T}} \quad \boldsymbol{\alpha}^{\mathrm{T}} \quad \mathbf{z}^{\mathrm{T}} \quad \Delta L \right]^{\mathrm{T}}$ denotes the vector of local unknowns, inferring that $\mathbf{r} = \mathbf{r}(\mathbf{X})$, and $\mathbf{J}^i$ is the local Jacobian matrix at iteration i of time t_{n+1} defined as $\mathbf{J}^i = \partial\mathbf{r}^i / \partial\mathbf{X}^i$, that is

$$\mathbf{J}^i = \begin{bmatrix} \partial\mathbf{r}_{\varepsilon^e}^i/\partial\boldsymbol{\varepsilon}^{e,i} & \partial\mathbf{r}_{\varepsilon^e}^i/\partial\boldsymbol{\alpha}^i & \partial\mathbf{r}_{\varepsilon^e}^i/\partial\mathbf{z}^i & \partial\mathbf{r}_{\varepsilon^e}^i/\partial\Delta L^i \\ \partial\mathbf{r}_{\alpha}^i/\partial\boldsymbol{\varepsilon}^{e,i} & \partial\mathbf{r}_{\alpha}^i/\partial\boldsymbol{\alpha}^i & \partial\mathbf{r}_{\alpha}^i/\partial\mathbf{z}^i & \partial\mathbf{r}_{\alpha}^i/\partial\Delta L^i \\ \partial\mathbf{r}_{z}^i/\partial\boldsymbol{\varepsilon}^{e,i} & \partial\mathbf{r}_{z}^i/\partial\boldsymbol{\alpha}^i & \partial\mathbf{r}_{z}^i/\partial\mathbf{z}^i & \partial\mathbf{r}_{z}^i/\partial\Delta L^i \\ \partial\mathrm{r}_{\Delta L}^i/\partial\boldsymbol{\varepsilon}^{e,i} & \partial\mathrm{r}_{\Delta L}^i/\partial\boldsymbol{\alpha}^i & \partial\mathrm{r}_{\Delta L}^i/\partial\mathbf{z}^i & \partial\mathrm{r}_{\Delta L}^i/\partial\Delta L^i \end{bmatrix} \tag{25}$$

which implies that the local Jacobian matrix is updated at each iteration. The components of the local Jacobian matrix are given in 'Appendix 2.' By finding the solution of the linearized system of Eq. (24), that is the increment of the elastic strain vector, the deviatoric back stress-ratio vector, the fabric-dilatancy vector, and the loading index $\left(\mathrm{d}\mathbf{X}^{i+1} = -\left(\mathbf{J}^i\right)^{-1} \cdot \mathbf{r}^i\right)$, the vector of local unknowns is updated using the following relation

$$\mathbf{X}^{i+1} = \mathbf{X}^i + \mathrm{d}\mathbf{X}^{i+1} \tag{26}$$

and the corresponding stress is computed from

$$\boldsymbol{\sigma}''^{,i+1} = \boldsymbol{\sigma}''_n + \mathbf{C}^{e,i+1} \cdot \Delta\boldsymbol{\varepsilon}^{e,i+1} \tag{27}$$

where $\Delta\boldsymbol{\varepsilon}^{e,i+1} = \boldsymbol{\varepsilon}^{e,i+1} - \boldsymbol{\varepsilon}^e_n$, and $\mathbf{C}^{e,i+1}$ is the elasticity matrix at iteration $i+1$ of time t_{n+1}, which is updated using

$$\begin{aligned} K^{i+1} &= \frac{2(1+\upsilon)}{3(1-2\upsilon)} G^{i+1}, \\ G^{i+1} &= G_0 p_{\mathrm{at}} \frac{(2.97-e)^2}{(1+e)} \left(\frac{p^{i+1}}{p_{\mathrm{at}}}\right)^{1/2} \end{aligned} \tag{28}$$

in which p^{i+1} is given by

$$p^{i+1} = \left(p_n^{1/2} - \frac{(1+\upsilon)}{3(1-2\upsilon)} \mathrm{G}_0 p_{\mathrm{at}}^{1/2} \frac{(2.97-e)^2}{(1+e)} \Delta\varepsilon_{\mathrm{v}}^{e,i+1} \right)^2 \tag{29}$$

where $\Delta\varepsilon_v^{e,i+1} = \mathrm{tr}\Delta\boldsymbol{\varepsilon}^{e,i+1}$. Hence, for the given strain increment $\Delta\boldsymbol{\varepsilon}$, a sequence of linearized system of equations is solved at each Gauss integration point until the iteration convergence is achieved. That is, the iterative process continues until the residual vector $\mathbf{r}^{i+1}$ vanishes within the

given tolerance, i.e., $\left\|\mathbf{r}^{i+1}\right\| \leq \text{Tol}$. A summary of the return mapping algorithm is given in Table 1.

4.2 Consistent tangent operator

It is well known that when a tangent operator consistent with the integration method employed for the numerical implementation of the elastoplastic constitutive model is used in the global Newton–Raphson algorithm to solve the system of equations resulting from the governing equations, the rate of convergence of the global iterative process is improved. In the following, a consistent tangent operator relevant to the return mapping algorithm presented in the foregoing subsection is derived.

The consistent tangent operator at time t_{n+1} is defined as $\mathbf{C} = \mathrm{d}\boldsymbol{\sigma}''/\mathrm{d}\boldsymbol{\varepsilon}$. In order to obtain a closed-form expression for the tangent operator consistent with the proposed return mapping algorithm, the chain rule is used

$$\mathbf{C} = \mathrm{d}\boldsymbol{\sigma}''/\mathrm{d}\boldsymbol{\varepsilon} = \mathrm{d}\boldsymbol{\sigma}''/\mathrm{d}\boldsymbol{\varepsilon}^e \cdot \mathrm{d}\boldsymbol{\varepsilon}^e/\mathrm{d}\boldsymbol{\varepsilon} \tag{30}$$

substituting $\mathrm{d}\boldsymbol{\sigma}''/\mathrm{d}\boldsymbol{\varepsilon}^e = \mathbf{C}^e$ into the above relation yields

$$\mathbf{C} = \mathbf{C}^e \cdot \mathrm{d}\boldsymbol{\varepsilon}^e/\mathrm{d}\boldsymbol{\varepsilon} \tag{31}$$

To derive a closed-form expression for $\mathrm{d}\boldsymbol{\varepsilon}^e/\mathrm{d}\boldsymbol{\varepsilon}$, the local residual vector at the converged state, $\mathbf{r} = \mathbf{0}$, is differentiated with respect to $\boldsymbol{\varepsilon}$. It is noted that at the global level $\mathbf{r} = \mathbf{r}(\mathbf{X}, \boldsymbol{\varepsilon})$, so its differentiation with respect to $\boldsymbol{\varepsilon}$ gives

$$\mathrm{d}\mathbf{r}/\mathrm{d}\boldsymbol{\varepsilon} = \partial\mathbf{r}/\partial\boldsymbol{\varepsilon} + \partial\mathbf{r}/\partial\mathbf{X} \cdot \mathrm{d}\mathbf{X}/\mathrm{d}\boldsymbol{\varepsilon} = \mathbf{0} \tag{32}$$

Table 1 Summary of the return mapping algorithm for the Manzari–Dafalias plasticity model

1. Begin elastic predictor phase in which we set

$\boldsymbol{\varepsilon}^{e,0} = \boldsymbol{\varepsilon}^{e,\text{tr}} = \boldsymbol{\varepsilon}_n^e + \Delta\boldsymbol{\varepsilon}$

$\boldsymbol{\alpha}^0 = \boldsymbol{\alpha}_n$

$\mathbf{z}^0 = \mathbf{z}_n$

$\Delta L^0 = 0.$

2. Compute stress $\boldsymbol{\sigma}''^{,0} = \boldsymbol{\sigma}''^{,\text{tr}} = \boldsymbol{\sigma}_n'' + \mathbf{C}^{e,0} \cdot \Delta\boldsymbol{\varepsilon}$.

3. Compute yield function $f\left(\boldsymbol{\sigma}''^{,0}, \boldsymbol{\alpha}^0\right)$.

If $f\left(\boldsymbol{\sigma}''^{,0}, \boldsymbol{\alpha}^0\right) \leq 0$, exit. Otherwise, set iteration counter $i = 0$ and continue.

4. Solve $\mathbf{J}^i \cdot \mathrm{d}\mathbf{X}^{i+1} = -\mathbf{r}^i$.

5. Update the vector of local unknowns using

$\mathbf{X}^{i+1} = \mathbf{X}^i + \mathrm{d}\mathbf{X}^{i+1}$.

6. Compute stress $\boldsymbol{\sigma}''^{,i+1} = \boldsymbol{\sigma}_n'' + \mathbf{C}^{e,i+1} \cdot \Delta\boldsymbol{\varepsilon}^{e,i+1}$.

7. Evaluate residual vector $\mathbf{r}^{i+1}$.

If $\left\|\mathbf{r}^{i+1}\right\| \leq \text{Tol}$, exit. Otherwise, set $i = i + 1$ and go to step 4.

in which $\partial\mathbf{r}/\partial\mathbf{X}$ is the local Jacobian matrix $\mathbf{J}$ evaluated at the locally converged state. Rearranging the above relation yields

$$\mathrm{d}\mathbf{X}/\mathrm{d}\boldsymbol{\varepsilon} = -\mathbf{J}^{-1} \cdot \partial\mathbf{r}/\partial\boldsymbol{\varepsilon} \tag{33}$$

from which a closed-form expression for $\mathrm{d}\boldsymbol{\varepsilon}^e/\mathrm{d}\boldsymbol{\varepsilon}$ is obtained as follows

$$\mathrm{d}\boldsymbol{\varepsilon}^e/\mathrm{d}\boldsymbol{\varepsilon} = [\mathbf{1} \quad \mathbf{0}] \cdot \mathrm{d}\mathbf{X}/\mathrm{d}\boldsymbol{\varepsilon} = -[\mathbf{1} \quad \mathbf{0}] \cdot \mathbf{J}^{-1} \cdot \partial\mathbf{r}/\partial\boldsymbol{\varepsilon} \tag{34}$$

in which $\mathbf{1}$ is the 6×6 identity matrix, $\mathbf{0}$ is the 6×13 zero matrix, $[\mathbf{1} \quad \mathbf{0}] \cdot \mathbf{J}^{-1}$ is equivalent to a submatrix corresponding to the first 6 rows of the inverse of the local Jacobian matrix and $\partial\mathbf{r}/\partial\boldsymbol{\varepsilon} = \left[(\partial\mathbf{r}_{\varepsilon^e}/\partial\boldsymbol{\varepsilon})^{\mathrm{T}} \quad (\partial\mathbf{r}_{\alpha}/\partial\boldsymbol{\varepsilon})^{\mathrm{T}} \quad (\partial\mathbf{r}_{z}/\partial\boldsymbol{\varepsilon})^{\mathrm{T}} (\partial\mathrm{r}_{\Delta L}/\partial\boldsymbol{\varepsilon})^{\mathrm{T}}\right]^{\mathrm{T}}$ whose components are given in 'Appendix 3.' Based on the above relation, a closed-form expression for the consistent tangent operator is obtained as

$$\mathbf{C} = -\mathbf{C}^e \cdot [\mathbf{1} \quad \mathbf{0}] \cdot \mathbf{J}^{-1} \cdot \partial\mathbf{r}/\partial\boldsymbol{\varepsilon} \tag{35}$$

5 Liquefaction criterion

In this section, a general, mathematical criterion for the onset of flow liquefaction instability is derived. The liquefaction criterion presented herein is on the basis of the pioneering work of Borja [5, 6], which is based upon the bifurcation theory. According to this theory, instabilities develop when the loss of equilibrium results in multiple feasible solutions [11].

Hill's loss of uniqueness or stability in the infinitesimal deformations case can be expressed as

$$[\![\dot{\boldsymbol{\sigma}}]\!]:[\![\dot{\boldsymbol{\varepsilon}}]\!] = 0 \tag{36}$$

where $[\![\dot{\boldsymbol{\varepsilon}}]\!] = \dot{\boldsymbol{\varepsilon}}^* - \dot{\boldsymbol{\varepsilon}}$ is the jump in the strain rate tensor due to potentially duplicate solutions for the velocity field and $[\![\dot{\boldsymbol{\sigma}}]\!] = \dot{\boldsymbol{\sigma}}^* - \dot{\boldsymbol{\sigma}}$ is the jump in the stress rate tensor. Hill's instability condition implies that uniqueness is lost or instability occurs when the jump in the stress rate tensor vanishes, that is $[\![\dot{\boldsymbol{\sigma}}]\!] = \mathbf{0}$. This means that the continuity of the stress rate tensor for a nonzero jump in the strain rate tensor results in the loss of uniqueness or stability. Using the definition of the total stress tensor and the constitutive equation $\dot{\boldsymbol{\sigma}}''=\mathbf{C}:\dot{\boldsymbol{\varepsilon}}$, the instability condition for the fully saturated case becomes

$$\mathbf{C}:[\![\dot{\boldsymbol{\varepsilon}}]\!] - \alpha[\![\dot{p}_w]\!]\mathbf{I} = \mathbf{0} \tag{37}$$

where $\mathbf{C} = \mathrm{d}\boldsymbol{\sigma}''/\mathrm{d}\boldsymbol{\varepsilon}$ is the consistent tangent and $[\![\dot{p}_w]\!]$ is the jump in the rate of the pore fluid pressure. It has been shown in [4] that the consistent tangent can be used instead of the continuum elastoplastic tangent $\mathbf{C}^{\text{ep}}$ for detecting the material instability.

The liquefaction instability is captured by the loss of uniqueness conditioned to the undrained bifurcation. To

impose this constraint, the jump in the Darcy's velocity vector of the fluid phase is forced to vanish, i.e., $[\![\dot{\mathbf{w}}_w]\!] = \mathbf{0}$. It is noted that the constraint of undrained bifurcation is not equivalent to the locally undrained condition, in which $\dot{\mathbf{w}}_w = \mathbf{0}$. That is, this criterion is expected to detect liquefaction instability not only in low permeability porous media, in which no significant drainage occurs, but also when the rate of loading is so rapid that excess pore water pressure develops before the pore water can drain away. In general, field-scale boundary value problems, all potential instabilities, e.g. instabilities in the form of strain localization (shear band) or drained diffuse instabilities, which are induced by kinematic constraints different from that observed in liquefaction instability, must be checked. Setting $[\![\dot{\mathbf{w}}_w]\!] = \mathbf{0}$ in the continuity equation of flow [Eq. (2)] yields the equivalent constraint for the liquefaction instability

$$\left(\frac{\alpha - n}{K_s} + \frac{n}{K_w}\right)[\![\dot{p}_w]\!] + \alpha[\![\dot{\varepsilon}_v]\!] = 0 \tag{38}$$

where $[\![\dot{\varepsilon}_v]\!]$ is the jump in the volumetric strain rate.

The loss of uniqueness [Eq. (37)] subject to the constraint obtained in Eq. (38) leads to

$$\begin{bmatrix} \mathbf{C} & -\alpha\mathbf{m} \\ -\alpha\mathbf{m}^{\mathrm{T}} & -\left(\frac{\alpha-n}{K_s} + \frac{n}{K_w}\right) \end{bmatrix} \begin{Bmatrix} [\![\dot{\boldsymbol{\varepsilon}}]\!] \\ [\![\dot{p}_w]\!] \end{Bmatrix} = \mathbf{0} \tag{39}$$

where $\mathbf{C}$ is the consistent tangent operator obtained in the previous section and $\mathbf{m}$ is the identity vector defined as $\mathbf{m} = [\,1 \quad 1 \quad 1 \quad 0 \quad 0 \quad 0\,]^{\mathrm{T}}$. For a nontrivial solution to exist, the determinant of the matrix, which is referred to as the liquefaction matrix $\mathbf{L}$, must vanish. Hence, liquefaction instability occurs when

$$\det \mathbf{L} = 0 \tag{40}$$

The above condition implies that liquefaction instability is predicted as a function of the state of the material, rather than the material property. The liquefaction criterion given above is general in the sense that it was derived without using any specific assumption. Moreover, it can be applied to any elastoplastic constitutive model, but it should be taken into account that the accuracy of the liquefaction prediction is highly dependent on the constitutive model used to simulate the mechanical behavior of the material. In the present work, the Manzari–Dafalias plasticity model is utilized, which is capable of simulating the behavior of granular materials under monotonic and cyclic loading conditions. Moreover, the precision with which the constitutive model is integrated has a significant effect on the accuracy of the liquefaction prediction. If the algorithm used for the numerical integration of the constitutive model involves numerical errors, the prediction of liquefaction instability will be as poor as the prediction of material behavior.

If the solid and fluid phases are incompressible, the liquefaction condition given in Eq. (39) becomes

$$\begin{bmatrix} \mathbf{C} & -\mathbf{m} \\ -\mathbf{m}^{\mathrm{T}} & 0 \end{bmatrix} \begin{Bmatrix} [\![\dot{\boldsymbol{\varepsilon}}]\!] \\ [\![\dot{p}_w]\!] \end{Bmatrix} = \mathbf{0} \tag{41}$$

where the last row of the liquefaction matrix implies the incompressible bifurcation, i.e., $[\![\dot{\varepsilon}_v]\!] = 0$. This means that for the incompressible solid and fluid phases, the constraint of undrained bifurcation ($[\![\dot{\mathbf{w}}_w]\!] = \mathbf{0}$) is equivalent to the constraint of incompressible bifurcation. The consequence of this constraint is that at the onset of liquefaction instability, the material deforms in the isochoric manner. The condition for liquefaction instability derived here is more general compared to that obtained by Andrade et al. [3], in which liquefaction instability is attained when the hardening modulus reaches the critical hardening modulus, in the sense that it was derived under conditions of triaxial (axisymmetric) loading, and incompressible solid and fluid phases. In general, it is well known that the instability criteria based on the constitutive tangent operator and critical hardening modulus are equivalent.

6 Numerical simulations

In this section, a number of examples are presented to verify the implicit return mapping algorithm developed for the Manzari–Dafalias plasticity model and to illustrate the predictive capability of the proposed liquefaction criterion under different loading conditions.

6.1 Monotonic undrained and drained triaxial tests on Toyoura sand

In order to verify the proposed numerical algorithm, a series of triaxial compression tests conducted by Verdugo and Ishihara [28] on Toyoura sand samples are simulated. These tests have been considered by various researchers to verify their numerical algorithm [9, 12]. In these test series, samples are loaded monotonically under undrained and drained conditions after consolidated isotropically, and then unloaded. Numerical simulation of these experiments is performed using the material subroutine inside the finite element code as well as the finite element analysis. Material parameters of the Manzari–Dafalias plasticity model used in the simulations for Toyoura sand are listed in Table 2.

Figure 1a, b shows the numerical and experimental results for a series of undrained triaxial compression tests conducted on isotropically consolidated samples of loose Toyoura sand ($e = 0.907$) with initial confining pressures ranging from $p = 100$ to 2,000 kPa. It is observed that when sheared under undrained conditions, loose Toyoura

Table 2 Material parameters of the Manzari–Dafalias plasticity model

	Toyoura sand	Nevada silty sand
Elasticity		
υ	0.05	0.05
G_0	125	125
Critical state		
M	1.25	1.45
c	0.712	1
e_{c0}	0.934	0.759
λ_c	0.019	0.0685
ξ	0.7	0.28
Yield surface		
m	0.01	0.01
Plastic modulus		
h_0	7.05	2.0
c_h	0.968	1.3
n^b	1.1	1.1
Dilatancy		
A_0	0.704	0.204
n^d	3.5	7.5
Fabric-dilatancy tensor		
c_z	600	500
z_{max}	4	10

sand samples exhibit contractive behavior together with softening. As expected for the undrained case and incompressible solid and fluid phases, void ratio remains constant during the simulation. Figure 1c, d shows the results for dense Toyoura sand samples with void ratio of $e = 0.735$ under undrained triaxial loading conditions. The initial confining pressure varies from $p = 100$ to 3,000 kPa. As expected for dense sand, the material undergoes the so-called phase transformation, which is a transition from contractive behavior to dilative behavior without softening. Figure 1e, f shows undrained triaxial test results for the case where the void ratio is equal to $e = 0.833$, and the initial confining pressure varies from $p = 100$ to 3,000 kPa. It is observed that for intermediate sand, depending on the initial confining pressure response of the same material varies from contractive response with softening to dilative response without softening, demonstrating the pressure-dependent behavior of sand. As expected, for undrained samples with the same void ratio, steady state is reached at the same point. Steady state is the state at large strains where continued straining does not produce further change in the stress state of the material.

Figure 2a, b shows the numerical and experimental results for a series of drained triaxial compression tests conducted on Toyoura sand samples with initial void ratios of $e = 0.831$, 0.917, 0.996. In all these cases, the initial confining pressure is equal to $p = 100$ kPa. As can be seen, depending on the state of the sand reflected in the state parameter samples shows different responses. In Fig. 2c, d, numerical results are indicated for a drained triaxial test series with a higher initial confining pressure of $p = 500$ kPa and different initial void ratios of $e = 0.810$, 0.886, 0.960. As can be seen, a similar trend is observed as with the previous test series upon reversal of loading in the sense that samples show contractive response during unloading. Compressing samples under drained conditions causes the void ratio to change, unlike the undrained case in which the void ratio remains constant. For both undrained and drained triaxial test series, it is observed that the obtained numerical results are in good agreement with the experimental ones, verifying our numerical implementation and showing the capability of the adopted constitutive model in capturing the main features of sand behavior.

In order to illustrate the capability of the presented criterion in capturing the onset of liquefaction instability, the sequence of undrained triaxial compression tests conducted on loose Toyoura sand samples ($e = 0.907$) with different initial confining pressures is considered. The deviatoric stress-axial strain diagrams and the effective stress paths are plotted in Fig. 3a, b, respectively. According to the experimental observations, liquefaction instability is attained at the maximum deviatoric stress point, marked by the circle symbol in Fig. 3a, b. It is observed that only samples with initial confining pressures of $p = 1{,}000$ and 2,000 kPa liquefy, and the sample with a relatively low confinement never liquefies. Indeed, two different types of behavior are observed. Loose samples with high confinement display high contractive tendency, causing the pore water pressure to increase continuously. The continuous increase in the pore water pressure is evidenced by the continuously decreasing mean effective stress. In this case, the samples undergo contractive behavior and deviatoric stress increases until liquefaction instability occurs at the peak point. After reaching the peak point, the behavior of the material becomes unstable in the sense that the deviatoric stress-axial strain diagrams and the effective stress paths exhibit a drop in the deviatoric stress. This unstable behavior continues until failure point or steady-state point is reached. At the failure point, the state of stress remains constant and does not change with further shearing. In contrast, the loose sample with low confinement encounters the so-called phase transformation and does not liquefy. In other words, at low confinement, the sample displays a reversal from contractive behavior to dilative behavior due to the low contractive tendency of sand at low confining pressures, directing the effective stress path to the right toward the failure point. In this case, the behavior of the material is always stable in the sense that the deviatoric

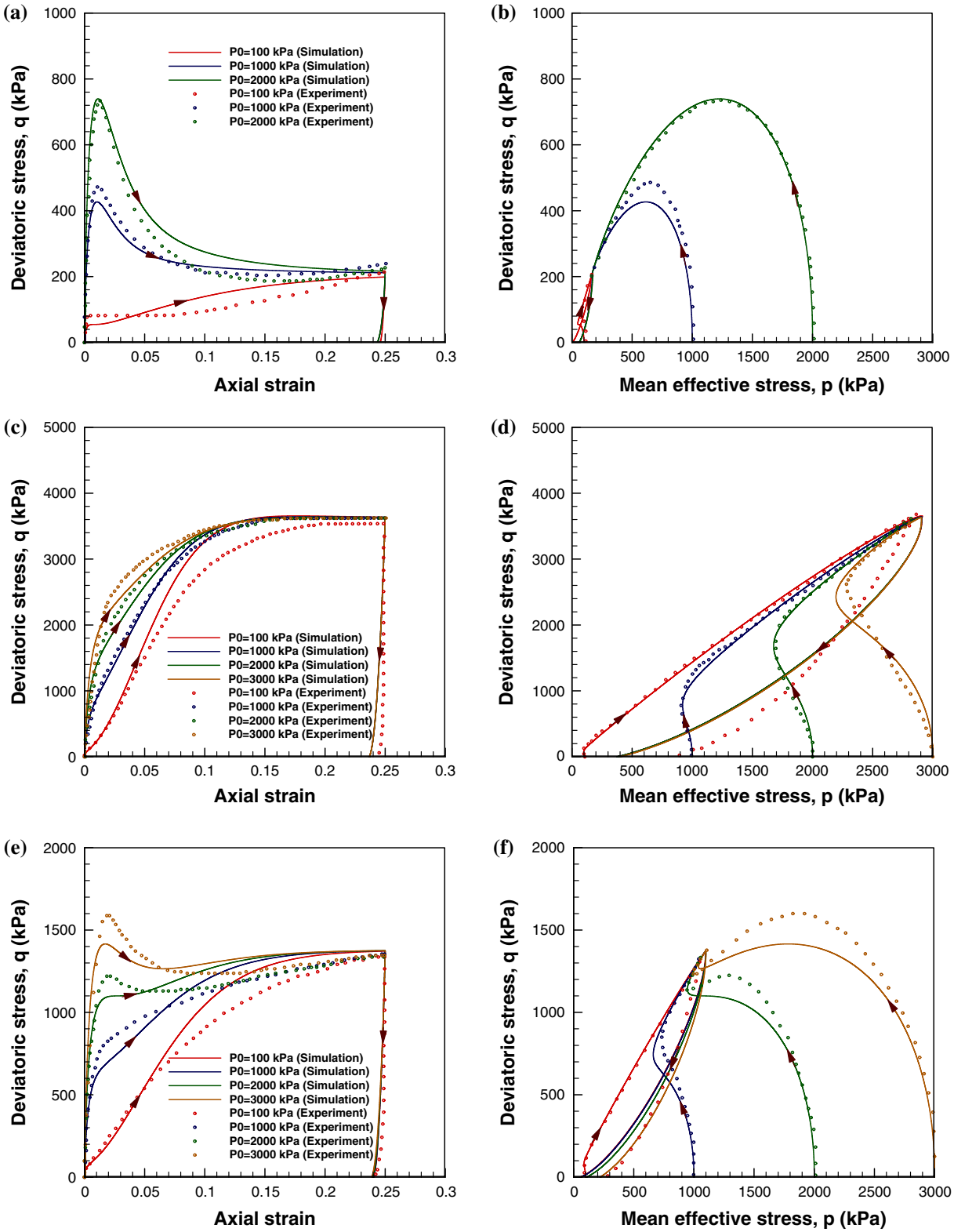

Fig. 1 Comparison between numerical and experimental results for the undrained triaxial compression test on samples of Toyoura sand with void ratios of **a**, **b** $e = 0.907$, **c**, **d** $e = 0.735$ and **e**, **f** $e = 0.833$

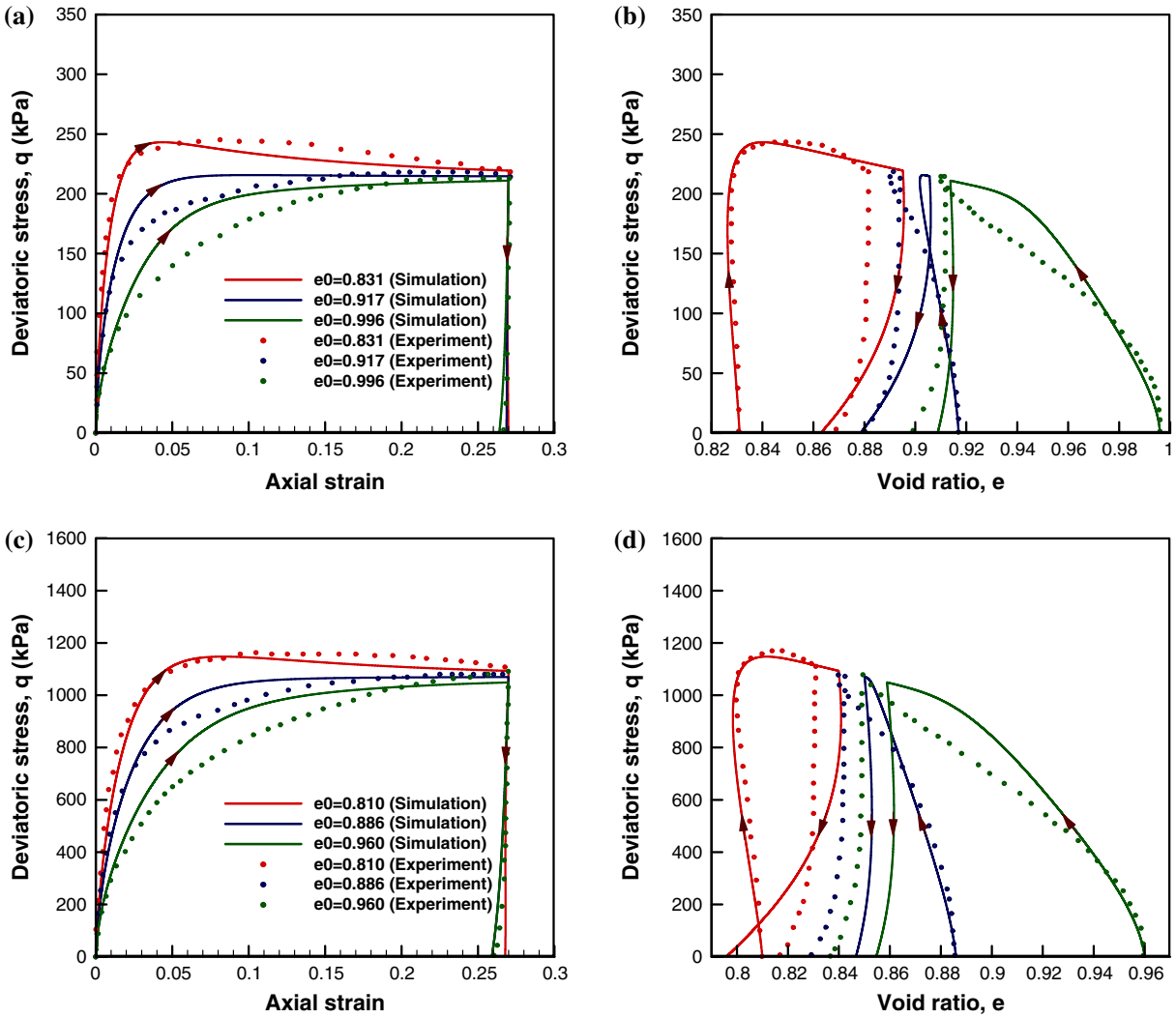

Fig. 2 Comparison between numerical and experimental results for the drained triaxial compression test on samples of Toyoura sand with initial confining pressures of **a**, **b** $p = 100$ kPa and **c**, **d** $p = 500$ kPa

stress-axial strain diagram and the effective stress path do not indicate a drop in the deviatoric stress. This stable behavior continues until failure occurs.

Figure 3c shows the evolution of the determinant of the liquefaction matrix. The onset of liquefaction instability is detected at the point where the zero axis is crossed. As can be seen, for the samples with high initial confinement the determinant of the liquefaction matrix obtained from Eq. (41) becomes equal to zero at the point corresponding to the peak point in the deviatoric stress-axial strain diagram and the effective stress path. For the sample with the initial confining pressure of p = 100 kPa, the determinant of the liquefaction matrix is entirely negative and never reaches zero. That is, the liquefaction criterion is never satisfied in this case, in accordance with the experimental observations. These results clearly demonstrate the efficiency of the presented criterion in capturing the liquefaction instability under monotonic loading conditions.

To assess the performance of the proposed implicit integration technique along with the consistent tangent operator, the local and global convergence profiles obtained from the finite element analysis of undrained triaxial compression test on Toyoura sand sample with initial confining pressure of $p = 1{,}000$ kPa and void ratio of $e = 0.907$ and drained triaxial compression test on Toyoura sand sample with initial confining pressure of $p = 500$ kPa and void ratio of $e = 0.960$ are presented. It is observed from Fig. 4a, c that for the given local tolerance (in these examples 10^{-12}), a few iterations are required to achieve the local convergence, and an asymptotic quadratic rate of convergence is obtained. As shown in Fig. 4b, d, using the consistent tangent operator, the

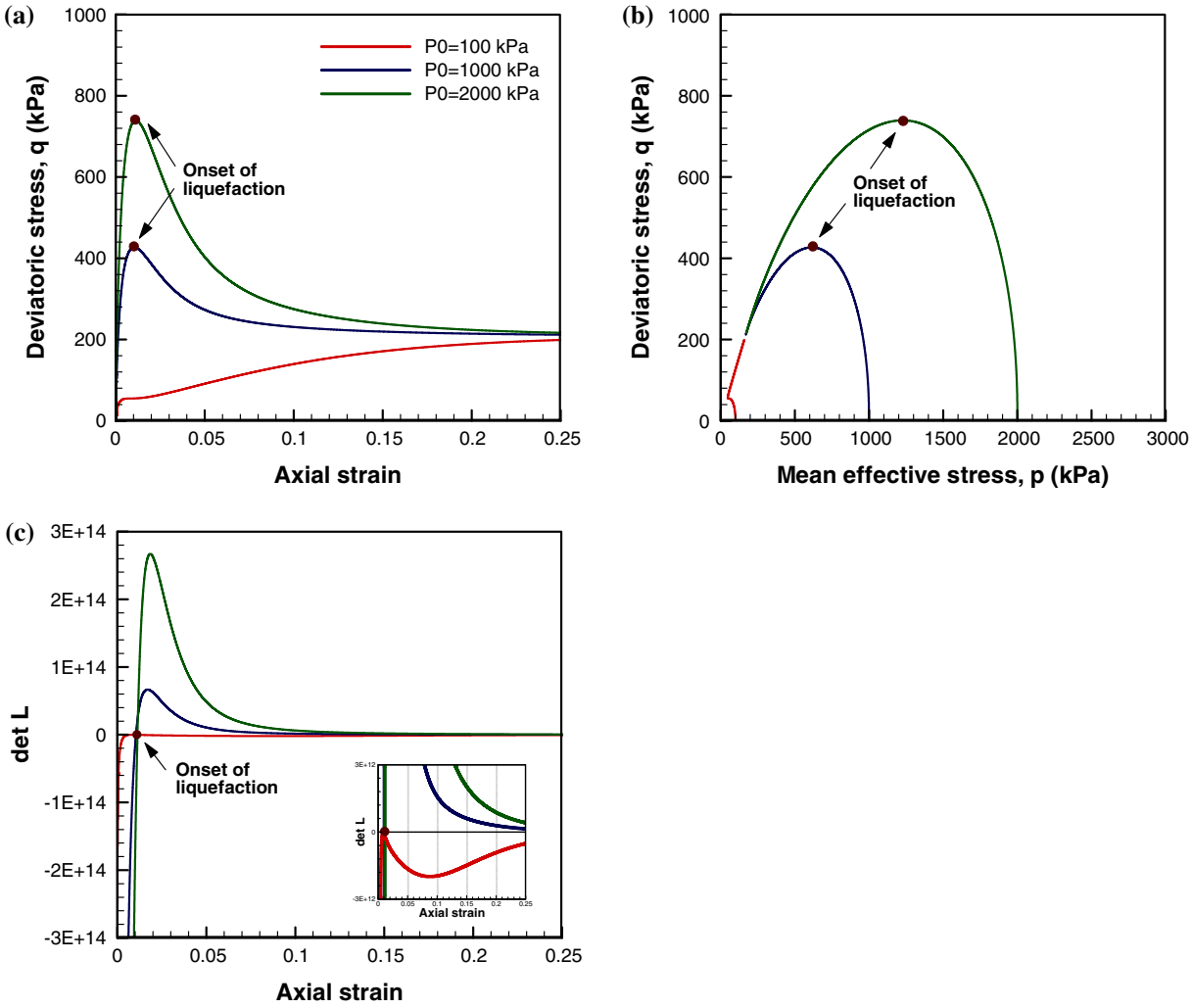

Fig. 3 Numerical results of the undrained triaxial compression test on samples of loose Toyoura sand with void ratio of $e = 0.907$

global residual vector vanishes within the given tolerance (in these examples 10^{-13}) after a few iterations. Moreover, the asymptotic quadratic convergence rate of the global Newton–Raphson iterative algorithm is preserved, demonstrating the computational efficiency of the proposed return mapping algorithm along with the consistent tangent operator in the solution of boundary value problems using finite elements.

It is worth mentioning that several monotonic undrained and drained triaxial tests were simulated using a broad range of increments to evaluate the performance of implicit and explicit integration schemes. It was observed that when very large increments are used, the implicit algorithm still provides solutions with reasonable accuracy, while the explicit algorithm fails to converge from the beginning when the increment size exceeds a certain intermediate value, indicating the accuracy of the implicit algorithm in a relatively wide range of increments. It was also observed that for the same increment size, the explicit algorithm requires less CPU time than the implicit algorithm. This is expected because of the heavy computational load required for the implicit algorithm. However, regarding that the explicit algorithm requires smaller increments compared to the implicit algorithm, the required CPU time of the two algorithms is comparable.

6.2 Cyclic undrained triaxial test on Toyoura sand

In this example, a comparison is made with the results reported in [9] for the cyclic undrained triaxial test conducted on a Toyoura sand sample with void ratio of $e = 0.808$. This example in fact illustrates the difference between liquefaction instability and cyclic mobility. First, the sample is consolidated isotropically to the confining pressure of $p = 294$ kPa (point A in Fig. 5a). Then, it is loaded cyclically under undrained conditions with the shear stress difference of 114.2 kPa. Fig. 5a shows the resulting effective stress path, in which the well-known butterfly

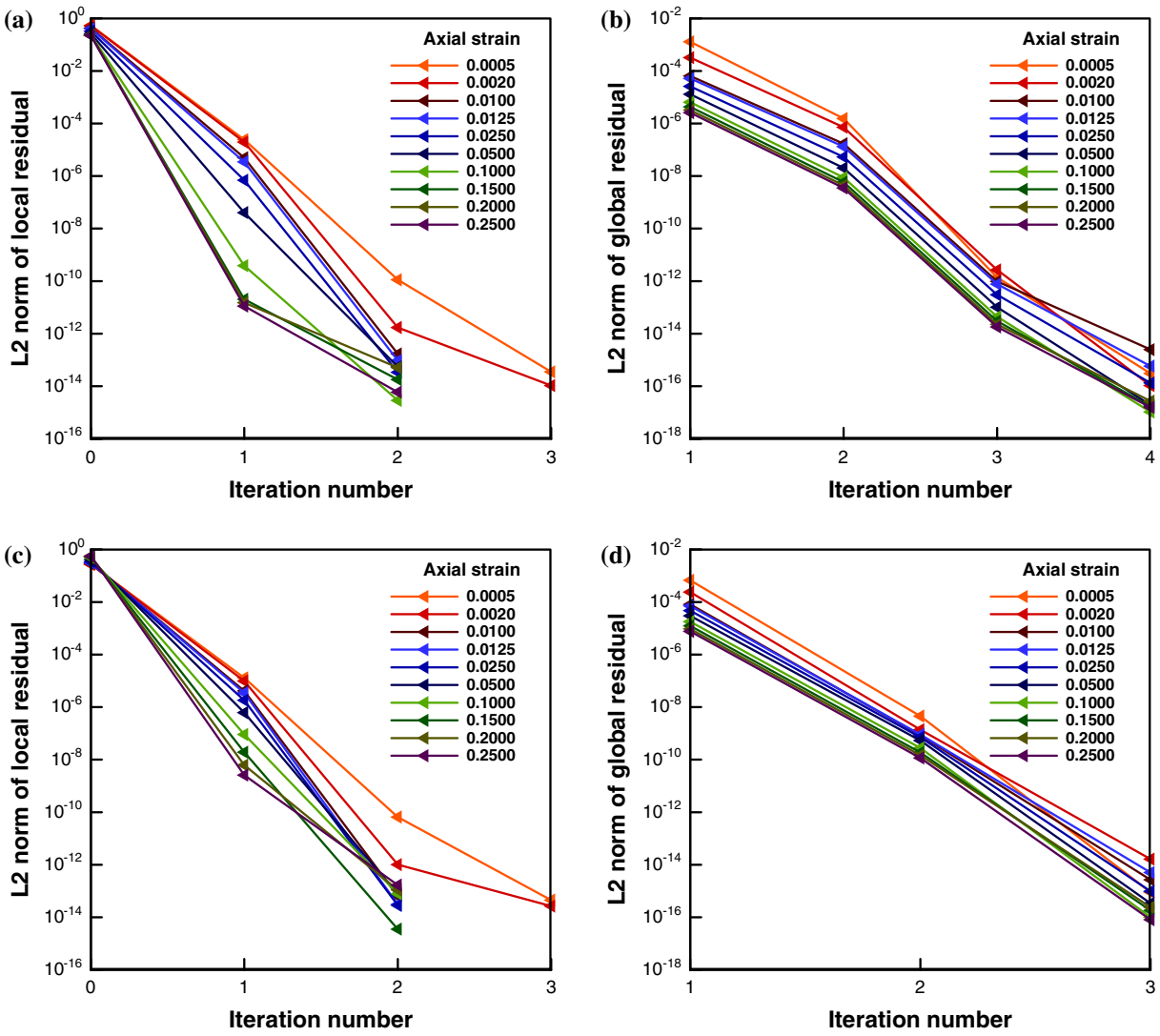

Fig. 4 Local and global convergence results at different axial strains for **a**, **b** undrained triaxial compression test on Toyoura sand sample with initial confining pressure of $p = 1{,}000$ kPa and void ratio of $e = 0.907$ and **c**, **d** drained triaxial compression test on Toyoura sand sample with initial confining pressure of $p = 500$ kPa and void ratio of $e = 0.960$

shape is formed. It is observed that there is a good agreement between the numerical results of ours and those reported in [9], verifying our numerical algorithm for cyclic loading.

It can be seen from the undrained effective stress path depicted in Fig. 5a that the sand behavior is always stable in the sense that the sand can sustain the constant deviatoric stress difference during the whole loading until the occurrence of failure. Consequently, the determinant of the liquefaction matrix obtained from Eq. (41) is always negative and never crosses the zero axis. That is, the liquefaction criterion is never satisfied, as shown in Fig. 5c. In fact, liquefaction instability never appears in this case although there is a decrease in the mean effective stress. This behavior is a typical behavior observed in experiments where cyclic mobility occurs, in which pore water pressure increases gradually with cyclic loading without exhibiting noticeable sudden changes in pore water pressure, and loss of controllability or instability is never observed [26]. This behavior contrasts with the characteristic behavior of flow liquefaction, which is associated with a sudden pore water pressure build-up and an occurrence of instability. In experiments exhibiting liquefaction, the sample displays an unstable behavior and failure follows, while in experiments with cyclic mobility the behavior is entirely stable until failure is reached. This example clearly shows that the proposed criterion can distinguish between liquefaction instability and cyclic mobility. Figure 5d shows the local convergence results of the proposed implicit integration scheme at several points, i.e., the loading reversal points

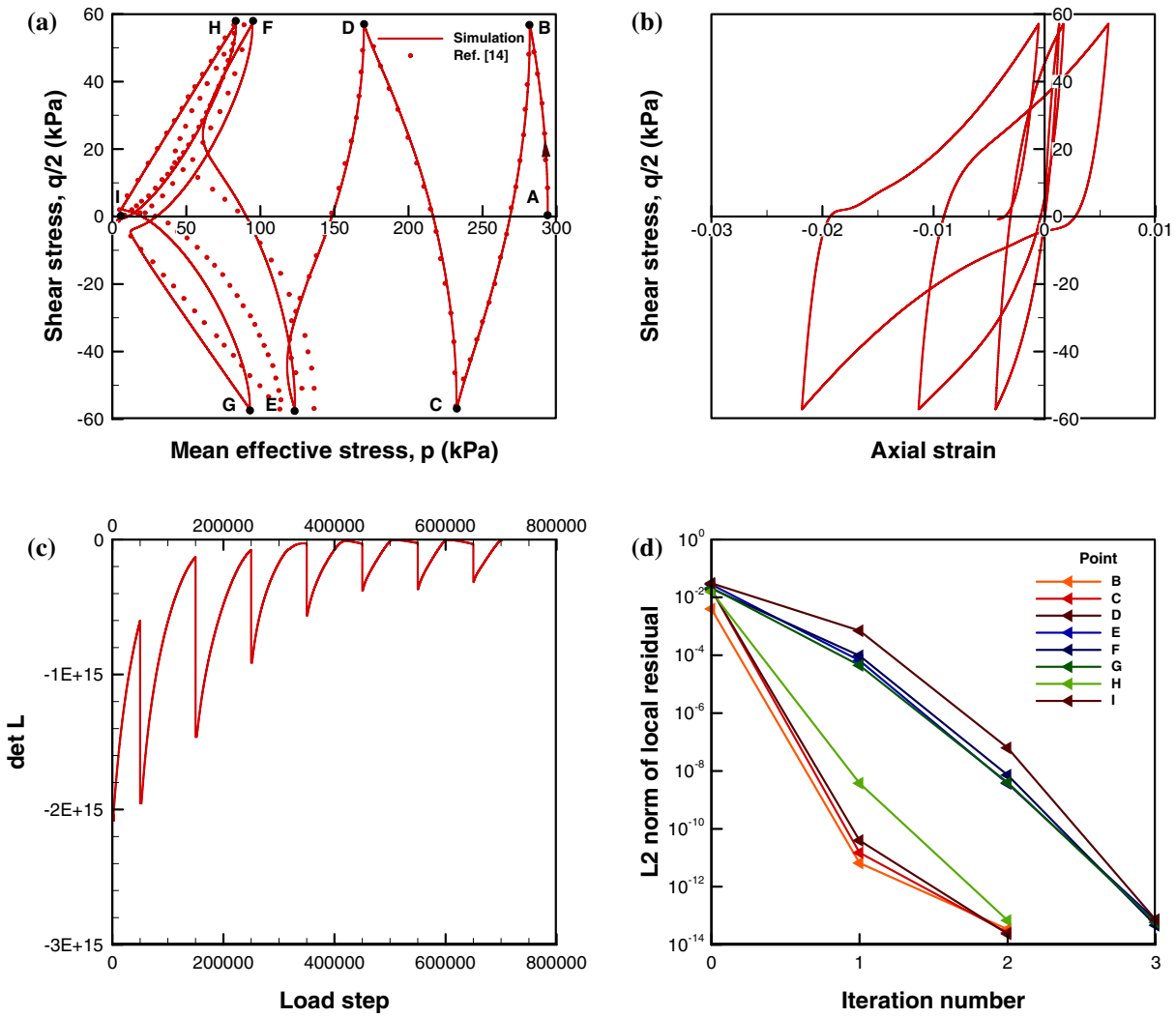

Fig. 5 Numerical results of the cyclic undrained triaxial test on Toyoura sand sample with void ratio of $e = 0.808$, initial confining pressure of $p = 294$ kPa and shear stress difference of 114.2 kPa for the case where the fabric-dilatancy variable is considered ($z_{max} = 4$)

and a stress point very close to the origin. As can be seen, a few iterations are required to achieve the local convergence within the given tolerance (in this example 10^{-12}). It is important to note that in the very low mean effective stress region, which is challenging from a numerical point of view, the presented implicit method is stable, and even at stress point I, the rate of convergence is asymptotically quadratic. This example was also simulated using the fully explicit method to test its stability. It was observed that the fully explicit method is unstable, and reducing the increment size does not prevent numerical instability.

6.3 Cyclic undrained triaxial test on Nevada silty sand

In this example, the cyclic undrained triaxial test conducted by Yamamuro and Covert [29] on Nevada silty sand is simulated. The material parameters of the Manzari–Dafalias plasticity model for the Nevada silty sand used in this numerical simulation are summarized in Table 2.

Initially, the specimen is consolidated isotropically until the effective confining pressure of $p = 225$ kPa is reached (point A in Fig. 6a). After isotropic consolidation, the specimen is sheared under drained conditions from the isotropic confining pressure of $p = 225$ kPa to the confining pressure of $p = 250$ kPa, which corresponds to the deviatoric stress of $q = 75$ kPa, i.e., from point A to point B. Along this portion, the effective stress path has a slope of 3, as expected for the drained triaxial compression test. Then, the specimen is turned undrained, and the cyclic undrained triaxial test is performed. During the cyclic loading, the mean effective stress decreases until the effective stress path reaches the point marked by the red

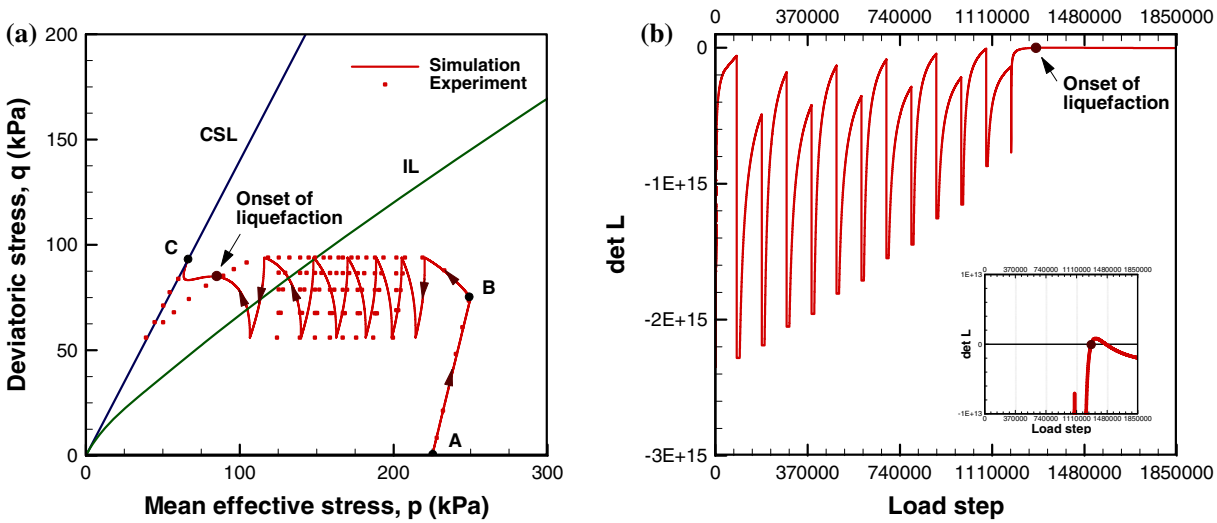

Fig. 6 Numerical results of the cyclic undrained triaxial test on Nevada silty sand sample with initial confining pressure of $p = 225$ kPa

circle in Fig. 6a. At this point, liquefaction instability occurs. After reaching this point, the constant deviatoric stress difference cannot be maintained, and the behavior of the material becomes unstable in the sense that the material cannot resist the constant deviatoric stress difference. Correspondingly, the determinant of the liquefaction matrix obtained from Eq. (41) becomes equal to zero at the point where liquefaction instability occurs as shown in Fig. 6b, demonstrating the capability of the criterion presented herein in detecting the onset of liquefaction instability under cyclic loading conditions. These results in fact show that the proposed criterion makes no distinction between monotonic and cyclic loading, implying that the liquefaction instability is a function of the state of the material, rather than the state of loading. Figure 6a also shows the CSL or the failure line as well as the instability line, which is the locus of points at which liquefaction instability is initiated under monotonic undrained triaxial loading conditions. The instability line is built by joining the peak points derived from a series of monotonic undrained triaxial compression tests with the same void ratio and different initial confining pressures. In this figure, the instability line is plotted for the case where the void ratio is the same as that of the cyclic undrained triaxial test. It is observed that the performed numerical simulation satisfactorily reproduces the experimental observations reported in [29].

6.4 Cyclic undrained plane strain test on Toyoura sand

In order to exemplify the applicability of the proposed liquefaction criterion to initial boundary value problems under dynamic loading conditions, an example is solved employing a fully coupled dynamic finite element analysis.

This example involves a fully saturated sample loaded dynamically under plane strain conditions. The geometry and boundary conditions of the problem are displayed in Fig. 7. As shown in this figure, the side length of the square sample is 1 m. The top boundary of the sample is loaded by a uniform vertical displacement that varies with time as $\bar{u}_y = 2 \times 10^{-3} \times 1.75^{\lfloor 5t \rfloor/2+1} \pi t \sin(5\pi t)$ m, where the symbol $\lfloor\rfloor$ denotes the greatest integer function. The side boundaries are subjected to a constant uniform confining pressure of 1,500 kPa. Undrained boundary condition is imposed on all boundaries of the sample. That is, the sample has impermeable boundaries to water. Prior to the dynamic loading, the sample is loaded monotonically under drained conditions from the isotropic confining pressure of $p = 1{,}500$ kPa to the state of stress marked by point A in Fig. 8a. The initial void ratio before the monotonic loading is $e = 0.909$. The computed effective stress and plastic internal variables at the end of the monotonic loading serve

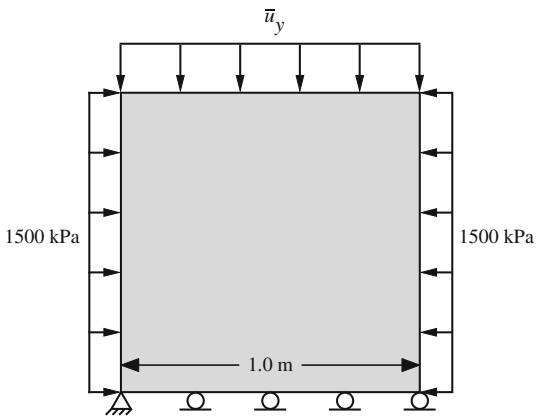

Fig. 7 Geometry and boundary conditions of the plane strain test

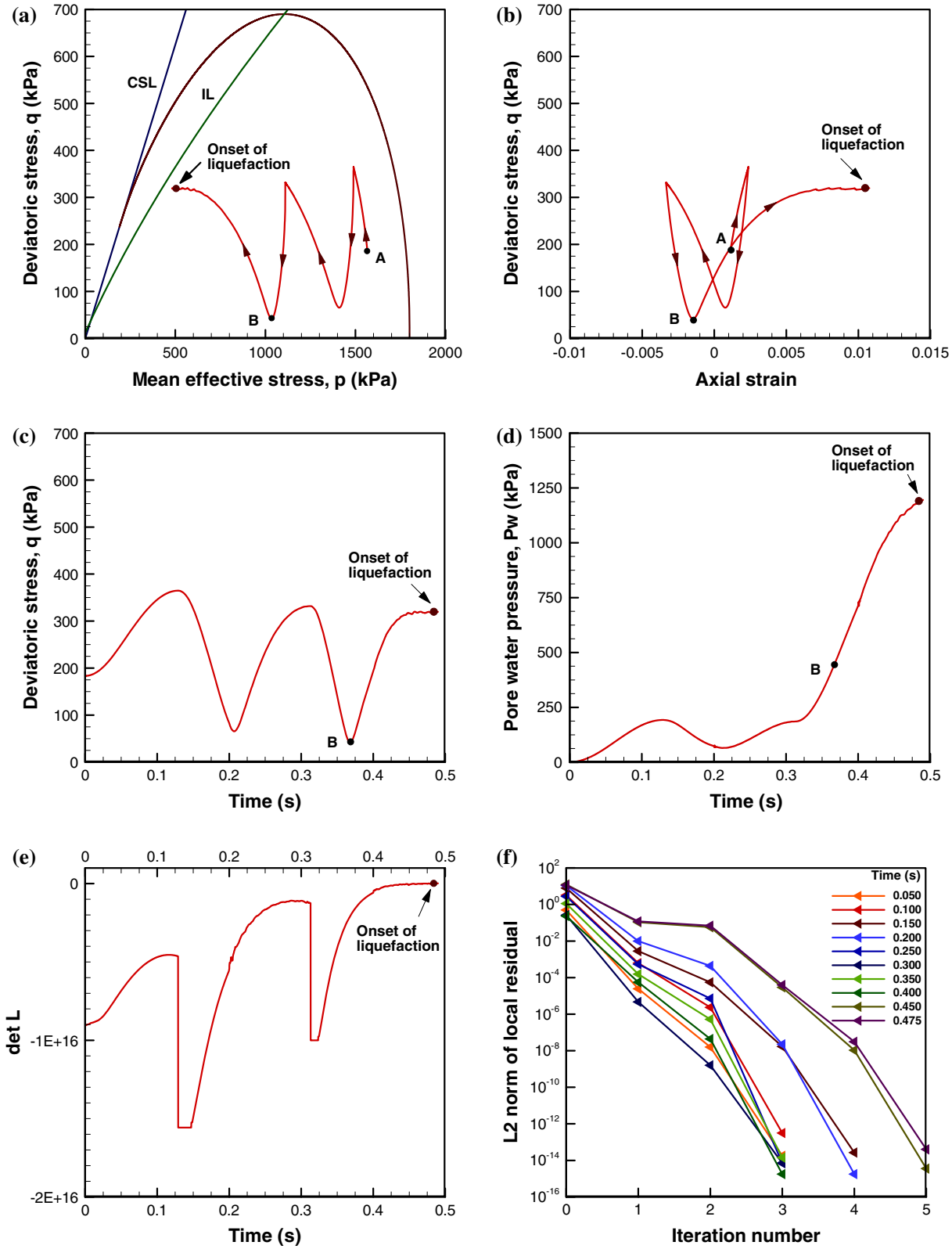

Fig. 8 Finite element results of the fully saturated sample loaded dynamically under plane strain conditions

Table 3 Material properties for the finite element analysis

Biot's constant	$\alpha = 1$
Solid phase density	$\rho_s = 2{,}000\,\mathrm{kg/m^3}$
Water density	$\rho_w = 1{,}000\,\mathrm{kg/m^3}$
Bulk modulus of solid phase	$K_s = 0.1 \times 10^{23}\,\mathrm{Pa}$
Bulk modulus of water	$K_w = 0.2 \times 10^{10}\,\mathrm{Pa}$
Intrinsic permeability	$k = 1 \times 10^{-10}\,\mathrm{m^2}$
Dynamic viscosity of water	$\mu_w = 1 \times 10^{-3}\,\mathrm{Pa\,s}$

as initial values to perform the dynamic analysis under cyclic loading. Indeed, the initial conditions for the dynamic analysis are obtained from a preliminary static drained analysis to ensure the satisfaction of mass and linear momentum balance equations at time $t = 0$. The adopted model parameters are assumed to be similar to those given in Table 2 for Toyoura sand. Material properties of the fully saturated soil considered in this example are listed in Table 3. The domain is discretized with 10×10 quadrilateral elements. The displacement field is approximated by biquadratic shape functions, and bilinear shape functions are used for the approximation of the water pressure field.

Figure 8a shows the effective stress path, surrounded by an envelope obtained from a monotonic undrained triaxial compression test for the same void ratio as in this example. It is noted that in this example, heterogeneity effects are negligible, and the material response is almost identical at all Gauss points. Therefore, the selected Gauss point is representative of the entire domain. It is observed that the sample reaches liquefaction instability very close to the instability line obtained from a series of monotonic undrained triaxial compression tests performed on samples with the same void ratio as in this cyclic test. However, neither the instability line nor the envelope serves as predictor for liquefaction. Figure 8d shows the evolution of the pore water pressure. As can be seen, during the first cycle the magnitude of the pore water pressure is not significant, but in the next cycle the pore water pressure increases suddenly. The sudden increase in the pore water pressure causes the mean effective stress to decrease remarkably, eventually resulting in the liquefaction instability. Accordingly, in the last cycle, the axial strain develops much more than the previous ones, as shown in Fig. 8b. Moreover, it maintains a nearly constant deviatoric stress until liquefaction instability takes place. The development of the pore water pressure and the subsequent drop in the mean effective stress continues before the onset of liquefaction instability. Accordingly, the determinant of the liquefaction matrix obtained from Eq. (39) becomes equal to zero at the point where the sample displays liquefaction instability, as observed from Fig. 8e. This example clearly indicates that liquefaction instability occurs when the aforementioned liquefaction criterion is met, proving the capability of the proposed criterion to capture liquefaction instability in boundary value problems under dynamic loading conditions. Figure 8f shows the local convergence results of the proposed return mapping algorithm at several times. It is observed that a few iterations are required to achieve the local convergence, and an asymptotic quadratic convergence rate is achieved for the given tolerance (in this example 10^{-12}).

7 Conclusions

In this paper, a general liquefaction criterion based on Hill's loss of uniqueness conditioned to the undrained bifurcation was presented for detecting the onset of liquefaction instability in fully saturated granular media. The Manzari–Dafalias plasticity model based on its recent modifications was employed to simulate the nonlinear behavior of granular materials. Furthermore, a fully implicit return mapping algorithm was developed for the numerical implementation of the Manzari–Dafalias plasticity model. It was shown that the local rate of convergence of the proposed implicit integration scheme is asymptotically quadratic. Moreover, in the finite element context when the consistent tangent operator is used in the solution of the governing system of equations, the performance of the implicit method is enhanced. That is, the asymptotic quadratic convergence rate of the global Newton–Raphson iterative process is preserved. It was observed that the presented implicit method is more accurate and stable than the explicit method. Relatively large increments deteriorate the numerical stability of the explicit method, while the implicit method produces accurate and stable solutions with relatively large increments. Moreover, the implicit method is able to provide converged solution in the very low mean effective stress region, while the explicit method fails to converge at low mean effective stress levels, and even a significant decrease in increment size does not ensure convergence.

The predictive capability of the liquefaction criterion presented herein was illustrated in several numerical simulations under both monotonic and cyclic loading conditions. It was shown that the proposed criterion is capable of capturing the onset of liquefaction instability under static

as well as dynamic loading conditions without resorting to any specific assumption and is able to distinguish between flow liquefaction and cyclic mobility. In cyclic mobility, pore water pressure increases gradually with cyclic loading without exhibiting noticeable sudden changes in pore water pressure, and loss of controllability or instability is not observed. Consequently, the liquefaction criterion is never satisfied in this case. In contrast, flow liquefaction is associated with a sudden increase in pore water pressure accompanied by unstable behavior. It is expected that the proposed framework can help advance our understanding of liquefaction and contribute to the repertoire of rational tools to predict the catastrophic effects of liquefaction instability in the long term.

Appendix 1

The coefficient matrices in the discretized governing Eq. (4) are given by

$$\begin{aligned}
\mathbf{M}_u &= \int_\Omega \mathbf{N}_u^{\mathrm{T}} \rho \mathbf{N}_u \mathrm{d}\Omega \\
\mathbf{M}_w &= \int_\Omega \nabla \mathbf{N}_{p_w}^{\mathrm{T}} \rho_w (\mathbf{k}/\mu_w) \mathbf{N}_u \mathrm{d}\Omega \\
\mathbf{Q} &= \int_\Omega \mathbf{B}^{\mathrm{T}} \alpha \mathbf{m} \mathbf{N}_{p_w} \mathrm{d}\Omega \\
\mathbf{C} &= \int_\Omega \mathbf{N}_{p_w}^{\mathrm{T}} \left(\frac{\alpha - n}{K_{\mathrm{s}}} + \frac{n}{K_w} \right) \mathbf{N}_{p_w} \mathrm{d}\Omega \\
\mathbf{H} &= \int_\Omega \nabla \mathbf{N}_{p_w}^{\mathrm{T}} (\mathbf{k}/\mu_w) \nabla \mathbf{N}_{p_w} \mathrm{d}\Omega
\end{aligned} \tag{42}$$

and the external force and flux vectors are given by

$$\begin{aligned}
\mathbf{F}_u &= \int_\Omega \mathbf{N}_u^{\mathrm{T}} \rho \mathbf{b} \, \mathrm{d}\Omega + \int_{\Gamma_t} \mathbf{N}_u^{\mathrm{T}} \bar{\mathbf{t}} \mathrm{d}\Gamma \\
\mathbf{F}_w &= \int_\Omega \nabla \mathbf{N}_{p_w}^{\mathrm{T}} \rho_w (\mathbf{k}/\mu_w) \mathbf{b} \mathrm{d}\Omega - \int_{\Gamma_{q_w}} \mathbf{N}_{p_w}^{\mathrm{T}} \bar{q}_w \mathrm{d}\Gamma
\end{aligned} \tag{43}$$

where $\mathbf{m}$ is the identity vector defined as $\mathbf{m} = [1 \;\; 1 \;\; 1 \;\; 0 \;\; 0 \;\; 0]^{\mathrm{T}}$, $\bar{\mathbf{t}}$ is the prescribed traction imposed on boundary Γ_t and $\bar{q}_w$ is the prescribed outflow imposed on the permeable boundary Γ_{q_w}.

Appendix 2

The components of the local Jacobian matrix $\mathbf{J}^i$ are given by

$$\begin{aligned}
\partial \mathbf{r}^i_{\varepsilon^e} / \partial \boldsymbol{\varepsilon}^{e,i} &= \mathbf{1} + \Delta L^i \partial \mathbf{R}^i / \partial \boldsymbol{\varepsilon}^{e,i} \\
\partial \mathbf{r}^i_{\varepsilon^e} / \partial \boldsymbol{\alpha}^i &= \Delta L^i \partial \mathbf{R}^i / \partial \boldsymbol{\alpha}^i \\
\partial \mathbf{r}^i_{\varepsilon^e} / \partial \mathbf{z}^i &= \Delta L^i \partial \mathbf{R}^i / \partial \mathbf{z}^i \\
\partial \mathbf{r}^i_{\varepsilon^e} / \partial \Delta L^i &= \mathbf{R}^i \\
\partial \mathbf{r}^i_{\alpha} / \partial \boldsymbol{\varepsilon}^{e,i} &= -\Delta L^i (2/3) \left(\mathbf{b}^i \otimes \partial h^i / \partial \boldsymbol{\varepsilon}^{e,i} + h^i \partial \mathbf{b}^i / \partial \boldsymbol{\varepsilon}^{e,i} \right) \\
\partial \mathbf{r}^i_{\alpha} / \partial \boldsymbol{\alpha}^i &= \mathbf{1} - \Delta L^i (2/3) \left(\mathbf{b}^i \otimes \partial h^i / \partial \boldsymbol{\alpha}^i + h^i \partial \mathbf{b}^i / \partial \boldsymbol{\alpha}^i \right) \\
\partial \mathbf{r}^i_{\alpha} / \partial \mathbf{z}^i &= \mathbf{0} \\
\partial \mathbf{r}^i_{\alpha} / \partial \Delta L^i &= -(2/3) h^i \mathbf{b}^i \\
\partial \mathbf{r}^i_{z} / \partial \boldsymbol{\varepsilon}^{e,i} &= c_z \Delta L^i \left(-H\left(-D^i\right) \left(z_{\max} \mathbf{n}^i + \mathbf{z}^i \right) \otimes \partial D^i / \partial \boldsymbol{\varepsilon}^{e,i} \right. \\
&\quad \left. + \langle -D^i \rangle z_{\max} \partial \mathbf{n}^i / \partial \boldsymbol{\varepsilon}^{e,i} \right) \\
\partial \mathbf{r}^i_{z} / \partial \boldsymbol{\alpha}^i &= c_z \Delta L^i \left(-H\left(-D^i\right) \left(z_{\max} \mathbf{n}^i + \mathbf{z}^i \right) \otimes \partial D^i / \partial \boldsymbol{\alpha}^i \right. \\
&\quad \left. + \langle -D^i \rangle z_{\max} \partial \mathbf{n}^i / \partial \boldsymbol{\alpha}^i \right) \\
\partial \mathbf{r}^i_{z} / \partial \mathbf{z}^i &= \mathbf{1} + c_z \Delta L^i \left(-H\left(-D^i\right) \left(z_{\max} \mathbf{n}^i + \mathbf{z}^i \right) \otimes \partial D^i / \partial \mathbf{z}^i \right. \\
&\quad \left. + \langle -D^i \rangle \mathbf{1} \right) \\
\partial \mathbf{r}^i_{z} / \partial \Delta L^i &= c_z \langle -D^i \rangle \left(z_{\max} \mathbf{n}^i + \mathbf{z}^i \right) \\
\partial \mathrm{r}^i_{\Delta L} / \partial \boldsymbol{\varepsilon}^{e,i} &= \mathbf{n}^i \cdot \partial \mathbf{s}^i / \partial \boldsymbol{\varepsilon}^{e,i} - \left(\boldsymbol{\alpha}^i \cdot \mathbf{n}^i + \sqrt{2/3} m \right) \partial p^i / \partial \boldsymbol{\varepsilon}^{e,i} \\
\partial \mathrm{r}^i_{\Delta L} / \partial \boldsymbol{\alpha}^i &= -p^i \mathbf{n}^i \\
\partial \mathrm{r}^i_{\Delta L} / \partial \mathbf{z}^i &= \mathbf{0} \\
\partial \mathrm{r}^i_{\Delta L} / \partial \Delta L^i &= 0
\end{aligned} \tag{44}$$

in which

$$\begin{aligned}
\partial \mathbf{R}^i / \partial \boldsymbol{\varepsilon}^{e,i} &= \mathbf{n}^i \otimes \partial B^i / \partial \boldsymbol{\varepsilon}^{e,i} + B^i \partial \mathbf{n}^i / \partial \boldsymbol{\varepsilon}^{e,i} + \left(\left(\mathbf{n}^i \right)^2 - (1/3) \mathbf{m} \right) \\
&\quad \otimes \partial C^i / \partial \boldsymbol{\varepsilon}^{e,i} + 2 C^i \mathbf{n}^i \cdot \partial \mathbf{n}^i / \partial \boldsymbol{\varepsilon}^{e,i} \\
&\quad - (1/3) \mathbf{m} \otimes \partial D^i / \partial \boldsymbol{\varepsilon}^{e,i} \\
\partial \mathbf{R}^i / \partial \boldsymbol{\alpha}^i &= \mathbf{n}^i \otimes \partial B^i / \partial \boldsymbol{\alpha}^i + B^i \partial \mathbf{n}^i / \partial \boldsymbol{\alpha}^i + \left(\left(\mathbf{n}^i \right)^2 - (1/3) \mathbf{m} \right) \\
&\quad \otimes \partial C^i / \partial \boldsymbol{\alpha}^i + 2 C^i \mathbf{n}^i \cdot \partial \mathbf{n}^i / \partial \boldsymbol{\alpha}^i \\
&\quad - (1/3) \mathbf{m} \otimes \partial D^i / \partial \boldsymbol{\alpha}^i \\
\partial \mathbf{R}^i / \partial \mathbf{z}^i &= -(1/3) \mathbf{m} \otimes \partial D^i / \partial \mathbf{z}^i \\
\partial h^i / \partial \boldsymbol{\varepsilon}^{e,i} &= h^i \left(\partial b^i_0 / \partial \boldsymbol{\varepsilon}^{e,i} - h^i \left(\boldsymbol{\alpha}^i - \boldsymbol{\alpha}_{\mathrm{in}} \right) \cdot \partial \mathbf{n}^i / \partial \boldsymbol{\varepsilon}^{e,i} \right) / b^i_0 \\
\partial h^i / \partial \boldsymbol{\alpha}^i &= -\left(h^i \right)^2 \left(\mathbf{n}^i + \left(\boldsymbol{\alpha}^i - \boldsymbol{\alpha}_{\mathrm{in}} \right) \cdot \partial \mathbf{n}^i / \partial \boldsymbol{\alpha}^i \right) / b^i_0 \\
\partial \mathbf{b}^i / \partial \boldsymbol{\varepsilon}^{e,i} &= \sqrt{2/3} \left(\mathbf{n}^i \otimes \partial \alpha^{b,i}_\theta / \partial \boldsymbol{\varepsilon}^{e,i} + \alpha^{b,i}_\theta \partial \mathbf{n}^i / \partial \boldsymbol{\varepsilon}^{e,i} \right) \\
\partial \mathbf{b}^i / \partial \boldsymbol{\alpha}^i &= \sqrt{2/3} \left(\mathbf{n}^i \otimes \partial \alpha^{b,i}_\theta / \partial \boldsymbol{\alpha}^i + \alpha^{b,i}_\theta \partial \mathbf{n}^i / \partial \boldsymbol{\alpha}^i \right) - \mathbf{1} \\
\partial D^i / \partial \boldsymbol{\varepsilon}^{e,i} &= \left(A_0 H \left(\mathbf{z}^i \cdot \mathbf{n}^i \right) \left(\mathbf{d}^i \cdot \mathbf{n}^i \right) \mathbf{z}^i - A^i_d \boldsymbol{\alpha}^i \right) \cdot \partial \mathbf{n}^i / \partial \boldsymbol{\varepsilon}^{e,i} \\
&\quad + \sqrt{2/3} A^i_d \partial \alpha^{d,i}_\theta / \partial \boldsymbol{\varepsilon}^{e,i} \\
\partial D^i / \partial \boldsymbol{\alpha}^i &= \left(A_0 H \left(\mathbf{z}^i \cdot \mathbf{n}^i \right) \left(\mathbf{d}^i \cdot \mathbf{n}^i \right) \mathbf{z}^i - A^i_d \boldsymbol{\alpha}^i \right) \cdot \partial \mathbf{n}^i / \partial \boldsymbol{\alpha}^i \\
&\quad + A^i_d \left(\sqrt{2/3} \partial \alpha^{d,i}_\theta / \partial \boldsymbol{\alpha}^i - \mathbf{n}^i \right) \\
\partial D^i / \partial \mathbf{z}^i &= A_0 H \left(\mathbf{z}^i \cdot \mathbf{n}^i \right) \left(\mathbf{d}^i \cdot \mathbf{n}^i \right) \mathbf{n}^i \\
\partial \mathbf{n}^i / \partial \boldsymbol{\varepsilon}^{e,i} &= \left(\partial \mathbf{s}^i / \partial \boldsymbol{\varepsilon}^{e,i} - \boldsymbol{\alpha}^i \otimes \partial p^i / \partial \boldsymbol{\varepsilon}^{e,i} - \mathbf{n}^i \right. \\
&\quad \left. \otimes \left(\mathbf{n}^i \cdot \partial \mathbf{s}^i / \partial \boldsymbol{\varepsilon}^{e,i} - \left(\boldsymbol{\alpha}^i \cdot \mathbf{n}^i \right) \partial p^i / \partial \boldsymbol{\varepsilon}^{e,i} \right) \right) / \left| \mathbf{s}^i - p^i \boldsymbol{\alpha}^i \right|
\end{aligned}$$

$$\begin{aligned}
\partial \mathbf{n}^i/\partial \boldsymbol{\alpha}^i &= -p^i\left(\mathbf{1}-\mathbf{n}^i\otimes\mathbf{n}^i\right)/\left|\mathbf{s}^i-p^i\boldsymbol{\alpha}^i\right| \\
\partial p^i/\partial \boldsymbol{\varepsilon}^{e,i} &= -K^i\mathbf{m} \\
\partial \mathbf{s}^i/\partial \boldsymbol{\varepsilon}^{e,i} &= -K^i/\left(2p^i\right)\Delta\mathbf{s}^i\otimes\mathbf{m}+2G^i(\mathbf{1}-(1/3)\mathbf{m}\otimes\mathbf{m})
\end{aligned} \tag{45}$$

where $\mathbf{1}$ is the 6×6 identity matrix, H is the Heaviside step function whose value is unity for positive arguments and zero otherwise, the symbol $|\ |$ denotes the L_2 norm of a vector, and the symbol $\otimes$ denotes the dyadic product of two vectors.

Appendix 3

The components of $\partial \mathbf{r}/\partial \boldsymbol{\varepsilon}$ are given by

$$\begin{aligned}
\partial \mathbf{r}_{\varepsilon^e}/\partial\boldsymbol{\varepsilon} &= -\mathbf{1}+\Delta L\partial\mathbf{R}/\partial\boldsymbol{\varepsilon} \\
\partial \mathbf{r}_{\alpha}/\partial\boldsymbol{\varepsilon} &= -\Delta L(2/3)(\mathbf{b}\otimes\partial h/\partial\boldsymbol{\varepsilon}+h\,\partial\mathbf{b}/\partial\boldsymbol{\varepsilon}) \\
\partial \mathbf{r}_{z}/\partial\boldsymbol{\varepsilon} &= c_z\Delta L(-H(-D)(z_{\max}\mathbf{n}+\mathbf{z})\otimes\partial D/\partial\boldsymbol{\varepsilon} \\
&\quad +\langle -D\rangle z_{\max}\partial\mathbf{n}/\partial\boldsymbol{\varepsilon}) \\
\partial \mathrm{r}_{\Delta L}/\partial\boldsymbol{\varepsilon} &= \mathbf{n}\cdot\partial\mathbf{s}/\partial\boldsymbol{\varepsilon}-\left(\boldsymbol{\alpha}\cdot\mathbf{n}+\sqrt{2/3}m\right)\partial p/\partial\boldsymbol{\varepsilon}
\end{aligned} \tag{46}$$

in which

$$\begin{aligned}
\partial\mathbf{R}/\partial\boldsymbol{\varepsilon} &= \mathbf{n}\otimes\partial B/\partial\boldsymbol{\varepsilon}+B\,\partial\mathbf{n}/\partial\boldsymbol{\varepsilon}+\left(\mathbf{n}^2-(1/3)\mathbf{m}\right) \\
&\quad \otimes\partial C/\partial\boldsymbol{\varepsilon}+2C\mathbf{n}\cdot\partial\mathbf{n}/\partial\boldsymbol{\varepsilon}-(1/3)\mathbf{m}\otimes\partial D/\partial\boldsymbol{\varepsilon} \\
\partial h/\partial\boldsymbol{\varepsilon} &= h(\partial b_0/\partial\boldsymbol{\varepsilon}-h(\boldsymbol{\alpha}-\boldsymbol{\alpha}_{\mathrm{in}})\cdot\partial\mathbf{n}/\partial\boldsymbol{\varepsilon})/b_0 \\
\partial\mathbf{b}/\partial\boldsymbol{\varepsilon} &= \sqrt{2/3}\left(\mathbf{n}\otimes\partial\alpha_\theta^b/\partial\boldsymbol{\varepsilon}+\alpha_\theta^b\partial\mathbf{n}/\partial\boldsymbol{\varepsilon}\right) \\
\partial D/\partial\boldsymbol{\varepsilon} &= (A_0H(\mathbf{z}\cdot\mathbf{n})(\mathbf{d}\cdot\mathbf{n})\mathbf{z}-A_d\boldsymbol{\alpha})\cdot\partial\mathbf{n}/\partial\boldsymbol{\varepsilon} \\
&\quad +\sqrt{2/3}A_d\partial\alpha_\theta^d/\partial\boldsymbol{\varepsilon} \\
\partial\mathbf{n}/\partial\boldsymbol{\varepsilon} &= (\partial\mathbf{s}/\partial\boldsymbol{\varepsilon}-\boldsymbol{\alpha}\otimes\partial p/\partial\boldsymbol{\varepsilon}-\mathbf{n} \\
&\quad \otimes(\mathbf{n}\cdot\partial\mathbf{s}/\partial\boldsymbol{\varepsilon}-(\boldsymbol{\alpha}\cdot\mathbf{n})\partial p/\partial\boldsymbol{\varepsilon}))/|\mathbf{s}-p\boldsymbol{\alpha}| \\
\partial p/\partial\boldsymbol{\varepsilon} &= (4.97+e)/(2.97-e)K\Delta\varepsilon_{\mathrm{v}}^e\mathbf{m} \\
\partial\mathbf{s}/\partial\boldsymbol{\varepsilon} &= (4.97+e)/(2.97-e)\left(-1+K\Delta\varepsilon_{\mathrm{v}}^e/(2p)\right)\Delta\mathbf{s}\otimes\mathbf{m}
\end{aligned} \tag{47}$$

References

1. Andrade JE (2009) A predictive framework for liquefaction instability. Geotechnique 59:673–682
2. Andrade JE, Borja RI (2007) Modeling deformation banding in dense and loose fluid-saturated sands. Finite Elem Anal Des 43:361–383
3. Andrade JE, Ramos AM, Lizcano A (2013) Criterion for flow liquefaction instability. Acta Geotech 8:525–535
4. Borja RI (2004) Computational modeling of deformation bands in granular media. II. Numerical simulations. Comput Methods Appl Mech Eng 193:2699–2718
5. Borja RI (2006) Condition for liquefaction instability in fluid-saturated granular soils. Acta Geotech 1:211–224
6. Borja RI (2006) Conditions for instabilities in collapsible solids including volume implosion and compaction banding. Acta Geotech 1:107–122
7. Castro G (1969) Liquefaction of sands. Harvard soil mechanics series, No 81. Pierce Hall
8. Choi CH (2004) Physical and mathematical modeling of coarse-grained soils. PhD Thesis, University of Washington, Seattle
9. Dafalias YF, Manzari MT (2004) Simple plasticity sand model accounting for fabric change effects. J Eng Mech 130:622–634
10. Ellison KC, Andrade JE (2009) Liquefaction mapping in finite-element simulations. J Geotech Geoenviron Eng 135:1693–1701
11. Hill R (1958) A general theory of uniqueness and stability in elastic-plastic solids. J Mech Phys Solids 6:236–249
12. Jeremić B, Cheng Z, Taiebat M, Dafalias Y (2008) Numerical simulation of fully saturated porous materials. Int J Numer Anal Methods Geomech 32:1635–1660
13. Khoei AR, Mohammadnejad T (2011) Numerical modeling of multiphase fluid flow in deforming porous media: a comparison between two- and three-phase models for seismic analysis of earth and rockfill dams. Comput Geotech 38:142–166
14. Kramer SL (1996) Geotechnical earthquake engineering. Prentice-Hall, Upper Saddle River, NJ
15. Lade PV (1992) Static instability and liquefaction of loose fine sandy slopes. J Geotech Eng 118:51–71
16. LeBlanc C, Hededal O, Ibsen LB (2008) A modified critical state two-surface plasticity model for sand—theory and implementation. DCE Technical Memorandum No. 8, Aalborg University
17. Lewis RW, Schrefler BA (1998) The finite element method in the static and dynamic deformation and consolidation of porous media. Wiley, New York
18. Li XS, Dafalias YF (2000) Dilatancy for cohesionless soils. Geotechnique 50:449–460
19. Li XS, Wang Y (1998) Linear representation of steady-state line for sand. J Geotech Geoenviron Eng 124:1215–1217
20. Manzari MT, Dafalias YF (1997) A critical state two-surface plasticity model for sands. Geotechnique 47:255–272
21. Manzari MT, Prachathananukit R (2001) On integration of a cyclic soil plasticity model. Int J Numer Anal Methods Geomech 25:525–549
22. Nova R (1994) Controllability of the incremental response of soil specimens subjected to arbitrary loading programmes. J Mech Behav Mater 5:193–201
23. Richart FE, Hall JR, Woods RD (1970) Vibration of soils and foundations. International series in theoretical and applied mechanics. Prentice-Hall, Englewood Cliffs, NJ
24. Schofield A, Wroth P (1968) Critical state soil mechanics. McGraw-Hill, New York
25. Seed HB, Lee KL, Idriss IM, Makdisi FI (1975) Dynamic analysis of the slide in the Lower San Fernando dam during the earthquake of February 9, 1971. J Geotech Eng Div 101:651–688
26. Toyota H, Nakamura K, Kazama M (2004) Shear and liquefaction characteristics of sandy soils in triaxial tests. Soils Found 44:117–126
27. Vaid YP, Sivathalayan S (2000) Fundamental factors affecting liquefaction susceptibility of sands. Can Geotech J 37:592–606
28. Verdugo R, Ishihara K (1996) The steady state of sandy soils. Soils Found 36:81–91
29. Yamamuro JA, Covert KM (2001) Monotonic and cyclic liquefaction of very loose sands with high silt content. J Geotech Geoenviron Eng 127:314–324
30. Zienkiewicz OC, Chan AHC, Pastor M, Paul DK, Shiomi T (1990) Static and dynamic behavior of soils; a rational approach to quantitative solution. I. Fully saturated problems. Proc R Soc Lond 429:285–309